Title
Global Health Diagnostics via Mobile Phone Microscopy: Improving Contrast and Resolution

Author
Friedman, Daniel Haim

Publication Date
2019

Peer reviewed|Thesis/dissertation

Global Health Diagnostics via Mobile Phone Microscopy: Improving Contrast and Resolution

by

Daniel Haim Friedman

A dissertation submitted in partial satisfaction of the

requirements for the degree of

Doctor of Philosophy

in

Bioengineering

in the

Graduate Division

of the

University of California, Berkeley

Committee in charge:

Professor Daniel A. Fletcher, Chair
Professor Chris J. Diederich
Assistant Professor Sarah A. Stanley

Spring 2019

Global Health Diagnostics via Mobile Phone Microscopy: Improving Contrast and Resolution

Abstract

Global Health Diagnostics via Mobile Phone Microscopy: Improving Contrast and Resolution

by

Daniel Haim Friedman

Doctor of Philosophy in Bioengineering

University of California, Berkeley

Professor Daniel A. Fletcher, Chair

A lack of access to proper disease screening and diagnostics continues to plague low-resource countries. As a result, diseases that have long been forgotten in affluent areas still cause an enormous, yet preventable burden in areas without adequate medical systems. In those countries, only the centralized healthcare facilities have the luxury of modern diagnostic equipment, along with the expert personnel required to use that equipment. Advances in consumer technologies, particularly the mobile phone, offer the potential to address the lack of access to healthcare in low-resource regions by creating new data collection and interpretation methods. One example with potential to improve disease diagnosis is the mobile phone microscope. By adding lenses to a conventional mobile phone camera, controlling sample illumination and motion, and automatically interpreting images, mobile phone microscopes have been shown to detect the presence of a pathogens and guide treatment decisions.

This thesis advances the state-of-the-art in mobile phone microscopy by introducing new applications, new contrast modalities, and resolution enhancements. First, I give an overview of the current prototype implementation of darkfield and fluorescence microscopy on a mobile phone microscopy platform developed by the Fletcher Lab, detailing the physical design of the system along with the assumptions and disadvantages associated with that design. I also show results of the microscope's initial on-site imaging of Fusarium at various banana plantations in the Philippines. Next, I introduce a new illumination scheme to overcome key limitations of the current implementation. I show that by using an LCD screen as the light source, it is possible to finely tune the illumination in a way that simultaneously captures uniform brightfield, darkfield, and phase contrast without the need for larger standard microscope optics. Finally, I take advantage of the smartphone's onboard image stabilizer to displace the sample image relative to the camera sensor. I use this displacement to demonstrate a simple dithering algorithm that requires no additional hardware while more than doubling the microscope's resolution. By combining these new methods, mobile phone microscopes of the future have the potential to provide high-quality disease diagnoses at the point-of-care.

Dedicated to Mom and Dad, who dedicated their lives to their kids. This is what you meant when you told me to be a doctor, right?

Contents

List of Figures

List of Tables

Acknowledgments

First, I want to thank my advisors throughout the years: Rick Van Berg, who took a chance on a high school student and opened so many doors in the process; Smita Sampath for pulling me into the world of medical imaging through MRI; Richard Carson for continuing my medical imaging training through PET; David Busch, Jen Lynch, Arjun Yodh, and Daniel Licht, who guided me through the world of diagnostics and gave me far more research freedom than an undergrad could hope to get; Steve Conolly and Chris Diederich, who introduced me to new fields of imaging and new schools of thought that I continue to use in every aspect of my research; and, of course, Dan Fletcher, who supported and guided me on my very windy path through the Ph.D.

I also want to thank all the amazing friends and labmates who rode along with me every step of the way. Michael Coppola and Katherine Han, who dealt with over a decade of unexpected 1am messages; the MEAM Fam at Penn – especially Sawyer Brooks, Justin Yim, Lev Avakian, Dean Wilhelmi, James Yang, and Cristina Sorice – without whom I would have never survived undergrad; the APO and Stouffer crew – especially Gloria Fann, Victoria Ng, Tiff Lu, and Annie Fu – who consistently challenged me to broaden my way of thinking, both in research and in life in general; and the SF crew – Jamin Liu, Joyce Chen, Andy Cheon, Vivian Look, Marissa Chou, Courtney Mazur, Jennifer Hu, Max Armstrong, Kathy Wei, Mike D'Ambrosio, and Karen Samy – who involuntarily became my "expert advice panel" throughout the Ph.D. And a special thanks to Amy Min and Michael Gil, who kept me on my feet and running in the right direction.

Finally, a huge thanks to my parents, Gad and Rachel Friedman, as well as my brothers, Tamir and Nizan Friedman. I can't even begin to list all the ways you've helped and guided me, but I can easily say I wouldn't be anywhere close to where I am now without you all.

Chapter 1

Introduction: Infectious Disease Diagnostics in Low-Resource Countries

Here in the US, along with most developed countries, the "getting sick" workflow is pretty straightforward. You start feeling off, you take some over the counter meds. If things don't get better, you go to your local doctor. If your doctor knows what's wrong, you get better meds. If not, you get a professional lab to poke you for samples, test those samples, and tell your doctor what's wrong. Then you get the better meds. Meanwhile, you go to local medical professionals–eye doctor, dentist, primary care physician, dermatologist–regularly to make sure anything you are unaware of gets caught as early as possible. And there's a good reason for this setup: it works. Early detection of disease drastically improves prognosis, as does prompt care once a disease is discovered [1].

Behind the scenes, a broader medical system is also at work, collecting data for analysis at a population level in order to detect rising epidemics and focus resources to areas that require them [2]. For instance, individuals who have never left the United States don't take any kind of medical prophylaxis for Malaria, because the population-level data makes it clear that malaria is not a risk to people in the US [3]. At the same time, individuals traveling to other countries that are known to host the pathogen are encouraged to take the prophylaxis, and even then, only if they are traveling in specific areas within a country that have recently shown notable rates of infection [4, 5]. This limits wasted resources in medical production, as well as wasted costs in the healthcare system as medicines are only prescribed when needed.

But there is a fatal flaw in this system: if even one component is missing or lacking, the workflow falls apart. What if you don't have money for medication? What if there is no local doctor, or no lab equipment to test you, or no expert to analyze the data? And what if there isn't a network in place for that data to go? While this dissertation focuses on diagnostic devices, it is important to go in with some baseline knowledge of how these gaps in a medical system affect a population and why.

1.1 Measuring the "Brokenness" of a Medical System

Let's start with statistics from high-income countries such as the US and most of Europe. On average, there are 5.7 hospital beds, 2.67 doctors, and 8.16 nurses per 1000 people [6, 7]. In total, the healthcare cost for those 1000 people amounts to approximately 3 million USD, only 20% of which is out-of-pocket [8]. To put those numbers in context, Africa in general had less than 0.1 hospital beds, 0.21 doctors, and 0.93 nurses per 1000 people: an order of magnitude difference. This makes sense given the average expenditure is over 100 times lower at less than 30USD per person. To make matters worse, 60% of those expenditures were out-of-pocket, meaning the people with the lowest levels of income are also the ones paying the most for their care [7, 8].

While the numerical differences are clear, the effects of those differences manifest in numerous ways, not all of which are intuitive. Developing countries regularly struggle with limited hours, long wait times, and low drug stocks at official health facilities [9–11]. This brings up a demand for cheaper, more available "health shops," which potentially provide medical services at lower prices [12]. One of the ways prices are lowered is by allowing for the purchase of incomplete drug regimens when a patient does not have the funds for the full course [13], which can lead to recurring issues as well as drug resistance [14–16]. Another major issue is that the little money available in the system will only afford the most centralized facilities with proper equipment such as diagnostic-grade microscopes, meaning only those in a population who have the financial means to travel for higher-level medical care are able to receive it [17]. This is one of the main arguments for developing low-cost portable devices that can provide central-health-center care at local health outposts.

1.2 Current State-of-the-Art in Mobile Microscopy

Difficulties in implementing traditional diagnostics in a low-cost and portable manner has led multiple groups to develop new ways to streamline the process. Microscopy has remained a major player in this space due to its inherent low per-test cost since slides and stains are, much of the time, significantly cheaper than the reagents required for biochemical assays [18, 19]. And while microscopy has historically required trained personnel to analyze the images, advancements in mobile processing have paved the way for more automated approaches [20, 21].

While by no means exhaustive, this section explores a list of groups that demonstrate key approaches that highlight the use of mobile microscopy.

The Ozcan Research Group

Ozcan et.al. have developed multiple implementations of a lensless mobile phone microscope [22, 23]). The microscopes are based on digital in-line holography, where a sample is placed 1-5mm away from a CMOS sensor and illuminated with partially coherent light [24, 25].

In this particular case, the illumination is generated by shining a single LED through a $50 - 100\mu m$ pinhole, positioned 40-100mm away from the sample. The CMOS sensor is the phone's embedded camera's sensor (with the lens module removed) [26]. The in-line holograms formed on the CMOS sensor are then run through an iterative phase recovery algorithm to generate an image of the sample [24, 25, 27].

Resolution is initially limited to the sensor's pixel pitch with a field of view approximately equal to the size of the sensor. However, by taking multiple images while inducing sub-pixel shifts in the position of the image with respect to the sensor (usually via multiple LED's to obtain multiple illumination angles), the group can synthesize full FOV images at approx. 500nm resolution [28]. This boosted resolution has allowed for imaging of extremely small samples, such as malaria parasites inside red blood cells. The group has produced multiple variations of this technology, with mobile versions designed for point-of-care applications such as blood counts and water-borne parasite detection [29, 30].

While a truly promising technology, the lensless approach does have key disadvantages for point-of-care use. This imaging technique requires extensive processing to generate useable images and currently requires offloading of data to either a laptop GPU or to the cloud. This becomes difficult when per-unit costs are expected to be minimal, and when access to stable high-speed internet is limited [24]. Furthermore, frame rates are typically 2-3fps while the super-resolution techniques used require between 10 and 80 images to be taken per acquisition (depending on the particular technique) [22]. Depending on how many acquisitions are necessary per diagnostic test, this could quickly become too time intensive for point-of-care use. Lastly, these methods require the phone itself to be permanently modified (removal of the camera lens), which limits the possibility of cost savings if users can be relied on to supply their own phone.

Prakash Lab

Prakash et.al. have developed an ultra-low cost portable microscope called the Foldscope [31]. While his lab is not dedicated to mobile microscopy, the Foldscope is worth mentioning due to its widespread use and publicity.

The Foldscope was designed with the main constraint of keeping the cost of parts under one US dollar [32]. The scope is constructed with a cheap ball lens, a coin cell battery, an LED (for transillumination), a switch, and copper tape. Everything is held together and aligned using card stock-thickness paper that has been precisely folded to allow for fine sample translation and focusing control in a hand-held manner. Magnification can be adjusted by switching between lenses of different radii. By adding gel filters or an additional ball lens with an annular aperture (to act as a darkfield condenser), the Foldscope can be cheaply converted into a low cost fluorescence or darkfield microscope [31].

The initial pilot program provided over 60,000 free Foldscopes to recipients in over 135 countries. These scopes were used in many low-resource applications such as identifying pest eggs in Indian agricultural areas and detecting bacteria in water supplies. Since then, a company has been formed around large scale production of the Foldscopes. They continue

to be used both for domestic applications (including sales as an educational kit) as well as in developing countries for parasite diagnostics, detection of fake currency and medicine, and similar applications [32].

While such a low-cost device clearly has its uses, the simplicity in the optics (i.e. use of a ball lens) creates aberrations that leaves most of the field of view unusable–as magnification increases, this effect worsens. This becomes especially true when used for machine learning-based applications, where uniformity across the field of view allows for simpler detection algorithms and smaller training sets. Despite that limitation, the Foldscope has clearly shown itself to be useful for applications that are simple enough for a human user to be inspecting a sample without the aid of digital analysis.

Wachsmann-Hogiu Lab

Wachsmann-Hogiu et.al. generally focus on molecular dynamics, cellular dynamics, and tissue diagnosis, but have developed multiple smartphone-based technologies as a result of their work [33–35]. The group first published on a mobile-phone microscope in 2011 using a 1mm ball lens mounted in front of the phone's camera lens [33] and illuminated by a diffused white LED. This imaging setup achieved $1.5\mu m$ resolution within a $150\mu m$ field of view. However, this system suffers from the same issues as mentioned above due to the aberrations introduced from the ball lens.

The group designed an updated system in 2019 which used an iPhone 6 screen as the illumination source, and an iPhone 5 lens in place of the ball lens [35]. The system achieved a resolution of $2\mu m$ with a field of view of 3.6mm x 2.7mm. By utilizing the high pixel density of the iPhone screen, the group was able to generate multiple illumination patterns to perform brightfield, darkfield, fluorescence, and Rheinberg contrast.

While the new setup has very promising utility, the methods described in the published work had several drawbacks. The contrast, especially for darkfield and Rheinberg, was far from consistent across the field of view, making only the very center comparable in performance to an equivalent microscope. Also, the limited brightness of a screen meant that many of the images taken, especially in fluorescence, required use of the maximum exposure setting of the phone (4 seconds), meaning any kind of scanning over large areas would quickly become time-prohibitive at the point-of-care. Nevertheless, the ability for high-detail solid-state structuring of illumination may provide a powerful tool for future diagnostics.

Oculyze

University labs are not the only players in the mobile microscopy space. Private companies are also developing field-applicable microscopes. One notable example is the German company, Oculyze [36]. Their strategy is to create a fully automated, easy-to-use microscope to allow for easier point-of-care diagnostics using blood samples. The idea is for the device to bridge the gap in infrastructure between the point of care and the central medical facilities.

The Oculyze mobile microscope is a self contained microscope with 400x magnification and a motorized stage. While the company is currently selling the device for yeast counting, plans are in place to move into the animal and human diagnostics sectors [37]. Users place a drop of blood on a slide and stain as necessary (for instance, a DNA stain for malaria). The slide is then placed on the microscope stage and illuminated with any light source. An external mobile device (phone, tablet, etc) connects to the microscope via USB and allows the user to trigger the camera. The mobile device then streams the data to the cloud for analysis by either physicians in a central facility, or by computer vision algorithms (note: this data pipeline has not yet been implemented). The results are sent back to the mobile device to guide the user on treatment options [36].

Unfortunately, this technology assumes a data connection will be available at the point of care, therefore limiting the areas where it could be useful. Also, the system still relies on the user being well-trained enough to be able to properly prepare the sample, which limits the usefulness of the automation. Without a production device available, it is difficult to know what niche this scope will fill, but the design ideology is promising

Fletcher Lab

Fletcher et.al. have developed multiple mobile devices based around directly using a mobile phone camera [38–42]. While varied, they roughly fall under two classes: objective based– essentially a "normal" microscope packaged into a portable format with either a phone or tablet placed at the eyepiece [38, 40, 42–44], and reversed lens based [39, 41, 45, 46]. The reverse lens system takes a duplicate smart phone lens (e.g. an iPhone 5s lens if using an iPhone 5s camera module) and places it in front of the of the built-in lens, but in a backward orientation [45]. This effectively created a tiny microscope with a magnification of 1X, meaning the resolution of the system is equal to the pixel pitch of the camera sensor (assuming the NA of the lens is high enough to keep the resolution as sampling limited and not diffraction limited).

So far, the largest project using this technology is the reversed-lens-based LoaScope, which has been used to test over 40,000 people in central Africa for filarial infections [39, 46]. The LoaScope is designed as a fully-automated system. Users draw blood via finger prick and touch a custom capillary to wick the blood into a specialized imaging chamber. The entire capillary is then inserted into the scope, which uses built-in illumination, a motorized carriage, and the reversed lens system to scan through the imaging chamber and image the blood. Motion maps are then generated, which allows an automated algorithm to count the number of moving worms in the blood. The scope then provides the number of microfilaria (normalized to microfilaria per mL of blood) and directs the user on whether or not to treat the patient.

With its current algorithm, the LoaScope is only capable of quantifying moving parasites, and can not distinguish between different species of parasite. It is also limited to the pixel pitch of the phone's sensor, which makes it the lowest resolution device on this list. That being said, there is nothing on the hardware side that is preventing the LoaScope from

utilizing significantly more complex computer vision algorithms to add still-parasite detection and morphological analysis for speciation. With the devices still in field use, there is a large potential for the LoaScope to grow into a more general diagnostic platform.

1.3 Advantages and Limitations of Phone-Based Microscopy

Thanks to market pressures and economies of scale, smartphones allow access to a portable system that encompasses a powerful processor, a multitude of sensors (accelerometer, thermometer, etc), and high-quality miniaturized optics, all for less than the cost of a reasonable quality low-end benchtop microscope [47]. However, in order to make full use of the system as a mobile microscope, it is important to understand how those miniaturized components work, and what tradeoffs were made in the process.

Smart Phone Digital Cameras

At the core, any digital camera is just an array of elements that convert photons into electrons. As of this writing, most smartphone camera sensors are complementary metal-oxide semiconductor (CMOS) image sensors, mainly due to their easy manufacturability and resulting low production cost (the sensor is basically an array of photodiodes and transistors printed on a silicon chip using the same methods used to produce microcontrollers, etc) [48].

One large tradeoff, however, is that CMOS sensors generally have a significantly lower fill factor (ratio of photosensitive area of a pixel to the full area of the pixel) than their more expensive charge coupled device (CCD) counterparts [49, 50]. Another tradeoff is in pixel size. While the race for having the "most megapixels" has mostly ended among the major smartphone manufacturers, the current standard is to cram 12 to 13 million pixels in an area between 9.9 and 22.6 square millimeters (the lower range being low-end smartphones like the Huawei Honor Lite series, and the upper end being the Samsung Galaxy S Series) [51]. This has led to pixel sizes on the order of 1 micron–great for achieving high image resolution with the LoaScope's reversed lens system, but troublesome from a noise and dynamic range standpoint.

The issue arises due to the nature of a pixel's full well capacity, or the amount of electrons it can hold before saturating, which is directly tied to the *active* surface area of the pixel (active being emphasized here since some of the area of a CMOS pixel is usually taken up by non-photosensitive components). Since number of electrons is tied directly to number of photons absorbed, this puts a limit on the number of photons absorbed before the pixel saturates. And since photon shot noise amplitude is simply the square root of the total number of photons absorbed, the small full well capacity leads to a very noisy image (compared to that of even a low-quality DSLR camera). Furthermore, since dynamic range (or a ability to see both bright and dark objects in the same photo without saturating or hitting the sensitivity floor of the sensor) is proportional to the full well capacity divided by the dark noise of

the sensor (an intrinsic property of the sensor that is independent of light input), a limited full well capacity also means these cameras tend to have very poor dynamic range. This is likely why almost every consumer camera now has a high-dynamic-range (HDR) mode, where the camera will take multiple exposures for a single photo and combine them into a final photo with an artificially boosted dynamic range. For those that are into photography, this is largely why a smartphone photo of the sun during sunset looks nothing like that taken by a DSLR.

Sensing Color

While not unique to smartphone cameras, color sensing adds an extra layer of complexity during image acquisition. It is necessary to understand how digital cameras "see" color when designing systems that requires post-processing of the image.

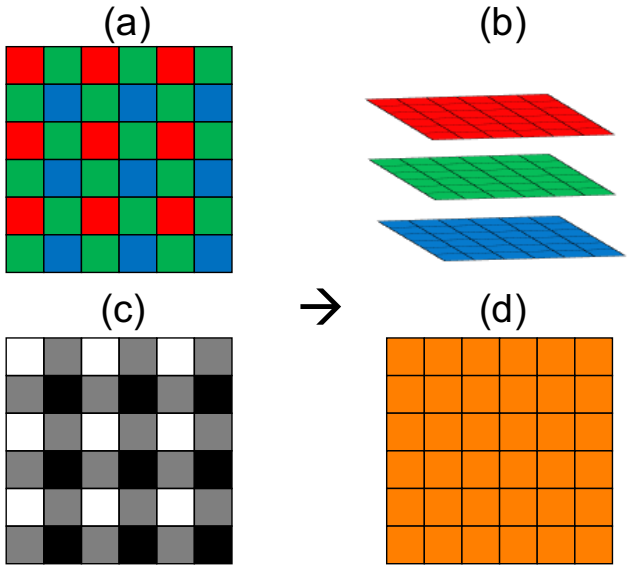

Figure 1.1: **Simplified bayer filter function.** (a) shows simulated color sensitivity of the bayer filter mask over the digital sensor. Note that each pixel only contains information about one of three color profiles (denoted by red, green, and blue colors in the diagram). Color information is then interpolated through a demosaicing algorithm to produce a red, green, and blue color value for each pixel (b). (c) simulates the raw information seen by the sensor for an orange image. This raw information is a single-layer grayscale image–color information is interpreted during the demosaicing step to produce the final color image (d).

The silicon section comprising the photodiode is sensitive to wavelengths of light between approx. 200nm to 1100nm [52]. In order to achieve the same color gamut as a human eye, color filters are placed over the pixels in a strategic pattern (see figure 1.1). This Bayer filter limits the sensitivity range of any particular pixel to roughly red, green, or blue light. Green

is used twice as often, in part, to mimic the human eye's heightened sensitivity to light in the green area of the visible spectrum [53].

Unfortunately, this also means that any particular pixel on the sensor only has information about one of the three colors. This leads to the necessary process of *demosaicing*, which uses information from surrounding pixels to assume what the value of that pixel would have been if it had the other two filters over it. This process transforms a greyscale $M\ x\ N$ image into a color $M\ x\ N\ x\ 3$ image, where each pixel has an associated red, green, and blue value. While outside the scope of this dissertation, it is worth noting that there exist a multitude of demosaicing algorithms, each with their own advantages and disadvantages in terms of color reproduction accuracy, performance at sharp edges, etc.

Smartphone Lenses

The lenses used in modern smartphones are a true marvel of engineering. Most brand name phone lenses have an aperture of f/2.4 (lower-end phones) [54–56] to f/1.8 (iPhone 8) [57] while maintaining distortion levels below 1% and virtually unnoticeable aberrations [47]. In less technical terms, phone lenses are capable of producing images with resolution on the order of $1\mu m$ while dimensionally remaining approximately within a 6mm cube.

Lens manufacturers achieve this performance by squeezing 4 to 6 elements within the package, most or all of which are aspheric on both sides [47]. From personal experience, trying to make a one-off lens group of similar size out of glass (excluding engineering time) would cost around $2000. Yet I'm able to purchase these phone lenses for less than $5 from Largan Precision suppliers at quantity 100. They achieve these price points by mass manufacturing millions of units, and injection molding most of the lenses out of plastic [47]. Usually, camera lenses are made out of glass to prevent aberrations/distortions from appearing due to thermal deformation–glass deforms very little between cold and hot conditions. But smartphone lenses escape this issue due to their size; even though plastic has much larger thermal deformations per unit temperature, those deformations are inconsequential with a <6mm lens [58].

This low cost is the heart of the LoaScope's reversed lens system. By using a flipped smartphone lens as an objective, it becomes very easy to make a low-cost, tiny, high-quality microscope. To put the values in perspective, a typical smartphone lens is 14 times less expensive and 145 times smaller (by volume) than a typical equivalent NA objective, all while achieving a field of view (FOV) over 5 times larger (see table 1.1 for details)[47, 59].

Using this type of lens does have a major disadvantage though: it is designed to create images with perspective (i.e. objects farther away are magnified less than objects close up). This makes sense: phone cameras are trying to mimic human perception of a scene. However, as will be discussed in detail in Chapter 2, this creates large challenges when attempting to use various illumination-based contrast modalities.

	Edmund Objective	Smartphone Lens
Field of View (mm)	2 (diameter)	4.8 x 3.6
Size (length/diameter in mm)	44/24	4/6.6
Cost (Quantity 1)	$110	$7.85

Table 1.1: **Comparison between a typical 10x/0.25NA plan objective (Edmund 43-907) and an equivalent NA smartphone lens (Largan Precision 6-element, <1% distortion lens).** FOV for Edmund lens is best-case measurement (i.e. though an eyepiece) to avoid the extra arguments about camera choice. Smartphone lens FOV is based off the sensor size it was designed for since it is practically limited to being used with smartphone cameras. Cost of smartphone lens is based on quotes from Largan Suppliers. [47, 59]

1.4 Dissertation Outline

The remainder of this dissertation explores the work done over the course of my Ph.D. to explore new contrast and resolution enhancements to the reversed-lens system, along with a brief field test of some of those enhancements. My goal was to organize the writing in a way that can be used as a general reference, and thus did my best to split each chapter into standalone sections where possible.

Chapter 2 explores current field implementations of three contrast modalities: brightfield, darkfield, and fluorescence. In this chapter, I break down each contrast modality and explain how they were implemented, why they worked, and what the main practical limitations of those implementations are. The chapter concludes with an example field trial, along with the background on the use case and the preliminary image results of the system.

Chapter 3 delves deeply into the difficulties of achieving uniform contrast with the reversed lens system. It also demonstrates a theoretical implementation to solve those issues and proves the solution works by achieving three different uniform contrast modalities (brightfield, darkfield, and phase) within a single image acquisition.

Chapter 4 moves away from contrast and instead focuses on resolution enhancement. The chapter explains the current issues limiting resolution and details a method for surpassing those limits using only the mobile phone's built in camera hardware.

Finally, Chapter 5 concludes the dissertation with a summary of the work done, along with my reflections on where that work can be best put to use at the point of care.

Chapter 2

Field Implementation of Simplified Multi-Contrast Imaging

This chapter focuses on practical implementation of multi-contrast imaging on a reversed-lens platform, both from a hardware complexity and timing standpoint. Specifically, brightfield, darkfield, and fluorescence are incorporated into the microscope as single-exposure modalities, though specific assumptions are taken into consideration. Thus, this chapter will focus on the basic concepts behind each of the three contrast modalities, how they are usually implemented, and how they are implemented in a reversed-lens microscope to identify a pathogen of banana plants with collaborators in the Philippines.

2.1 Brightfield Illumination

Brightfield contrast is characterized by dark objects against a bright background. The more an object absorbs light, the darker it becomes, and the higher contrast it has against the background. The reverse is also true: if an object does not significantly absorb light (e.g. a flat cheek cell), it will be almost invisible in brightfield (assuming it is in focus).

The way to achieve brightfield illumination is to ensure that the light hitting sample is traveling at a shallow enough angle relative to the objective's field angle such that it is accepted through the objective's aperture (see figure 2.1). For the usual microscope objective, finding the correct illumination angles is trivial. The field angle is zero degrees everywhere in the field of view, so the maximum illumination angle accepted is the arcsine of the numerical aperture (NA) of the objective. Thus, illumination comprised of all the angles below that defined by the objective NA will provide brightfield contrast.

Unfortunately, as alluded to in the previous chapter, the non-telecentric reversed lens does not behave as nicely. The field angle increases from the center to the edge of the field of view. In practice, that means that a specific angle of light may be within the brightfield region for certain parts of the field of view, but will never be in the brightfield region for the entire field of view. For example (in a 1D case for simplicity), if the maximum acceptance

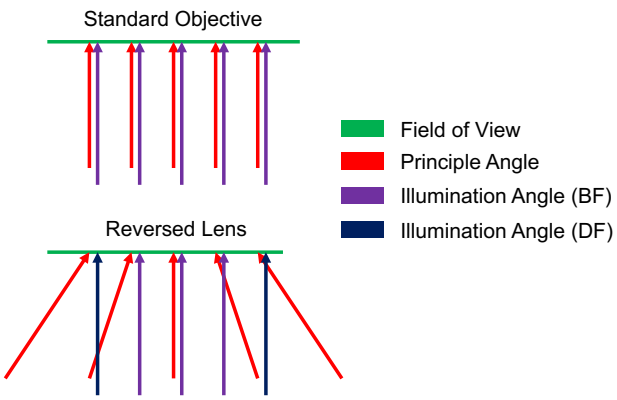

Figure 2.1: **Simplified diagram of acceptance angles for standard objectives vs reversed lens system.** Both diagrams show a sample (green) being illuminated by a single plane wave at 0 degree incidence (blue if the light angle is at a small enough angle to be accepted by the lens, purple if it is not). The red arrows depict the local principle angle. The aperture of the objective lens limits the angle between the illumination and principle angles. This angle remains constant with a standard objective, but varies across the field of view for the reversed lens system.

angle is 10 degrees (NA = .17) and the illumination angle is 10 degrees, everywhere in the field of view with a field angle of 0 degrees to 20 degrees will be in brightfield contrast, but everywhere outside of that section of the field of view will not.

It is also worth noting that pure brightfield illumination should be axisymmetric (e.g. if a sample is illuminated at +10 degrees, it should also be illuminated at -10 degrees). However, in this example, the only point that is symmetrically illuminated is the point in the FOV corresponding to a field angle of 10 degrees; the rest of the field of view will be asymmetrically illuminated, leading to phase artifacts in the image.

Practical Implementation

The solution, in this case, ends up being quite simple: illuminate from every angle necessary to ensure every point in the field of view is fully lit in brightfield. Working off the previous example, if the lens had a maximum field angle of 30 degrees, then the illumination would be composed of all angles of light between -40 and 40 degrees (max field angle plus max acceptance angle; see figure 2.2). The LoaScope achieves this illumination profile with a diffused white LED array positioned approximately a centimeter under the sample holder [39].

Note that this setup also means that every part of the field of view is also simultaneously in darkfield contrast (discussed in more detail in the following section). Since brightfield features are dark against the background, but darkfield features are bright against the background, the two contrast mechanisms somewhat cancel each other out, reducing the overall

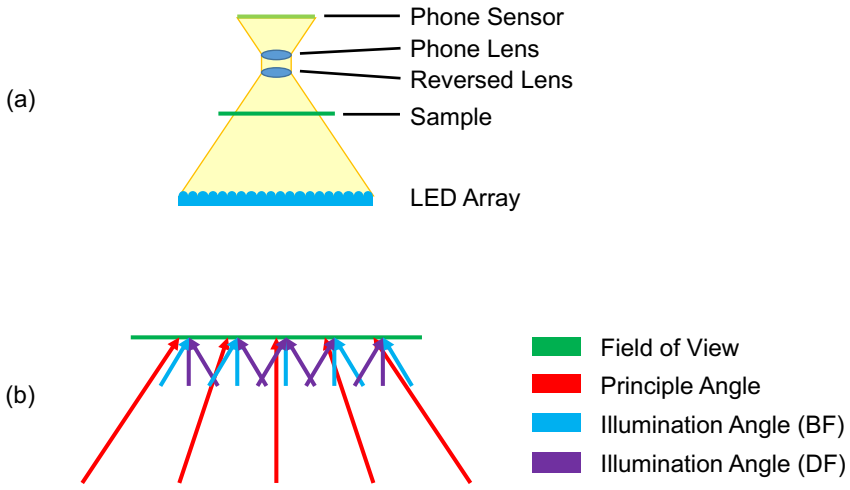

Figure 2.2: **Practical implementation of brightfield illumination.** (a) shows a simplified diagram of the reversed lens optical train with brightfield illumination. An LED array illuminates the sample with a wide variety of angles. (b) shows the resulting illumination acceptance across the field of view. All areas of the field of view have at least some illumination angles within the brightfield acceptance range, but all areas also have at least some amount of darkfield illumination as well.

contrast of the image. However, it can generally be assumed that the darkfield contributions are significantly dimmer than the brightfield contributions; so while the darkfield does theoretically deteriorate the image, the effects are not noticeable in most samples (at least, samples that are suitable for viewing in brightfield in the first place).

2.2 Darkfield Illumination

Achieving uniform darkfield illumination is a much more difficult task. Whereas brightfield relies on the sample absorbing light, darkfield relies on the sample scattering light (this is a fairly substantial oversimplification, but works for the purposes of analyzing possible illumination techniques. Look into Abbe Theory for a more complete view of darkfield illumination from a Fourier prospective). The intensity of the scattered light is almost always lower than that of a brightfield background, which means that no brightfield light can be allowed while generating a darkfield image. Instead, the sample needs to be illuminated with only non-brightfield light (e.g. from our previous example, the center of the FOV would be illuminated from angles of -10 degrees and below, and +10 degrees and above; see figure 2.3).

In Chapter 2, this was achieved by taking hundreds of images with different angles, and throwing away all the parts of the FOV in each image that were in brightfield. In practice, it would be best to have a single-shot modality to reduce acquisition and processing

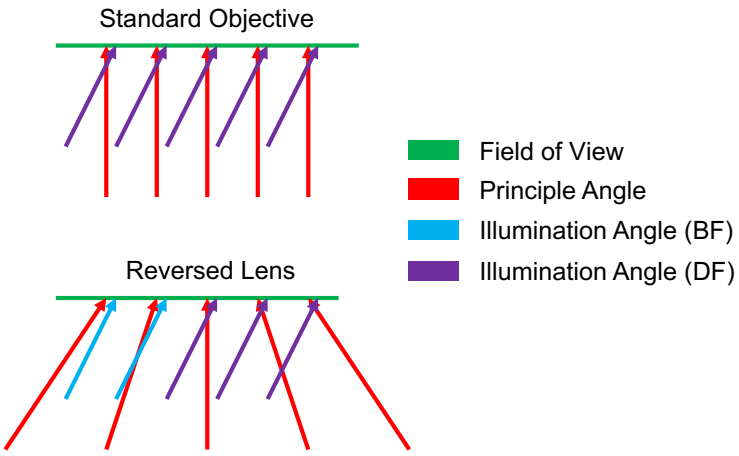

Figure 2.3: **Simplified diagram of darkfield angles for standard objectives vs reversed lens system.** Darkfield relies on the illumination angle being high enough relative to the principal angle that the light is does not pass through the aperture. For a standard objective, an illumination angle that is rejected by the objective aperture in one location of the FOV will be rejected for all locations on the FOV. With the reversed lens, the same issue arises where angles that are in darkfield for one region of the FOV will become brightfield in other regions.

time (especially for moving samples, which would flat out fail to work in the patch-based illumination scheme). To do this, the angles of illumination used must be outside of the brightfield range for every point in the field of view.

For a typical reversed lens setup (NA = 0.25), this corresponds to a minimum angle of around 55 degrees (max acceptance angle of approx. 15 degrees plus a max field angle of approx 40 degrees). However, darkfield brightness drops as the local illumination angle (illumination angle minus field angle) increases, which means the brightness of an object my vary significantly depending on where it is in the FOV, leading to potential issues in image underexposure/saturation. Also, given size constraints, creating a ring of illumination at 55 degrees or more is a very difficult task. Thus, a few key assumptions are made:

- Areas with a local illumination angle close to the maximum brightfield angle will be near the edge of the FOV, where vignetting is significant.
- Vignetting will offset the largest brightness discrepancies, leading to a relatively uniform brightness across the FOV.
- Using just one very high angle of illumination along the long axis of the image will be uniform enough for diagnostic purposes.

That last one is admittedly more of a necessity than an assumption, but can be true in practice (as will be discussed later in the chapter). With those assumptions in mind,

the darkfield illumination was designed with one white LED illuminating the sample at 60 degrees (see figure 2.4).

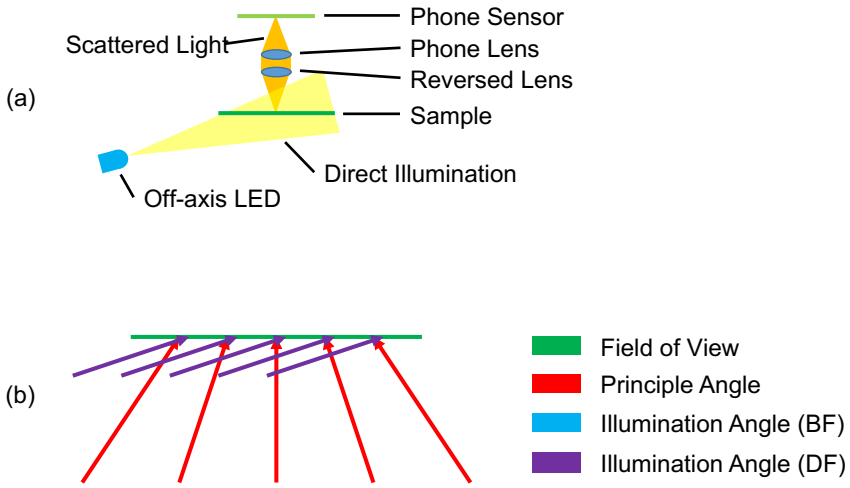

Figure 2.4: **Practical implementation of darkfield illumination.** (a) demonstrates the applied darkfield setup, where a high power LED shines on the sample from an angle high enough that no light is accepted through the lens aperture. Thus, any signal detected by the phone's sensor is from areas of the sample that have scattered the illumination light. (b) shows why this setup can work. Although the apparent illumination angle is changing throughout the field of view, the illumination angle remains high enough that no part of the field of view can accept it.

One last point to bring up is the issue of reflection artifacts. Some angles of light outside the brightfield range end up reflecting off the internal walls of the lens, creating large areas of high background. Each model lens seems to have different angles at which this affect occurs, but every lens we tested has this issue. It is therefor extremely important to test the lens that will be used in the final product and choose a darkfield illumination angle that does not cause this issue.

2.3 Fluorescence Illumination

Fluorescence illumination was by far the most difficult modality to achieve in the reversed lens system. The issues arise due to the compact nature of the optics: (1) The working distance is on the order of 300 microns, so there is virtually no free space between the objective and the sample, and (2) any space between the reversed lens and the camera lens results in substantial vignetting. The low dynamic range of the sensor also creates saturation and noise floor issues. Let's take a step back to understand how each issue arrises and can be compensated for.

Background Theory

From an oversimplified perspective, fluorescence microscopy is accomplished by shining light (excitation) at a fluorescent sample, and then picking out the light emitted from the sample (emission). See figure 2.5 for an example range of excitation and emission spectra. Note that the excitation light and the emission light must be at different wavelengths to be able to separate the sample light from excitation light. One of the simplest implementations of fluorescence imaging is a transillumination setup:

1. A broadband light source is shined through a filter (excitation filter–usually an interference filter) to narrow the bandwidth of the light.

2. The light is focused onto the sample through a condenser lens (usually by focusing the light source image onto the back focal plane of the condenser to achieve uniform illumination on the sample).

3. The light hits the sample and excites the fluorophores, which then emit light evenly in all directions

4. The emission light and excitation light are collected by the objective and run through a second filter (emission filter–again usually an interference filter) which does not have any overlap in transmission with the excitation filter, yet still allows as much light as possible through from the emission spectrum of the fluorophores.

5. The remaining light is then either imaged through the microscope eyepiece or onto a camera. If done correctly, the image should show where on the sample fluorescent light has been emitted.

The main issue with this type of setup is the difficulty in finding filters that can adequately eliminate enough light from the system. While no filter is perfect, the goal is to eliminate enough excitation light that it is lost in the noise floor of the detector, even while properly exposing for the emission signal. Given that the excitation for many fluorescent samples can be over six orders of magnitude brighter than the emission, solution to this challenge can be quite expensive.

That is partly why one of the most common ways fluorescence imaging is done is by an epifluorescence setup:

1. A broadband light source is shined through an excitation filter

2. The light bounces off a beam splitter and focuses on the back focal plane of the microscope objective (essentially using the objective as a condenser lens).

3. The light hits the sample and excites the fluorophores

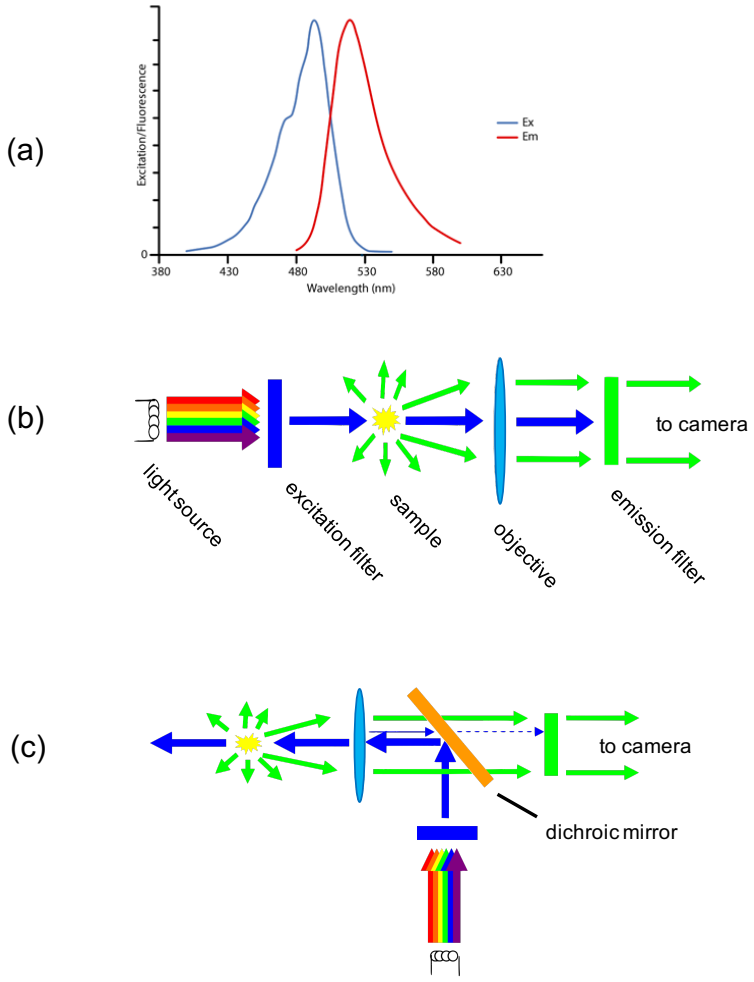

Figure 2.5: **Fluorescence setup diagrams.** (a) Sample excitation/emission graph (Alexa 488 courtesy of Jackson ImmunoResearch Laboratories [60]). (b) Example diagram of an transillumination fluorescence setup courtesy of Switz, Fletcher. Broadband light (rainbow arrows) is filtered through an excitation filter and hits the sample (yellow). The sample emits light (green arrows) in all directions, some of which is picked up by the objective lens. All light travels through the emission filter to remove the collected excitation light. The remaining light is imaged onto a sensor. (c) Example diagram of an epifluorescence setup courtesy of Switz, Fletcher. Broadband light is filtered through an emission filter, then bounced off a 45 degree dichroic mirror (orange) into the back of the objective. The objective then focuses the light onto the sample, which emits light in all directions. Some of the emission light, along with scattered excitation light, is collected by the same objective and runs through the dichroic mirror and emission filter before being imaged onto the sensor.

4. The emission light and *scattered* excitation light are collected by the objective and hit the beam splitter again. The light that bounces off is discarded, while the light that flows through the splitter is run through an emission filter.

5. The remaining light is then either imaged through the microscope eyepiece or onto a camera.

Epifluorescence has one main advantage for the purposes of this discussion: the vast majority of the excitation light never even makes it to the emission filter, since only light that scattered/reflected off the sample can make it back. That makes it easier to find a filter that can push the excitation intensity down to the noise floor while maintaining a proper exposure of the emission.

Unfortunately, this system requires an objective that can image the sample onto a sensor several centimeters away. Every phone lens we have worked with has needed the sensor within 1mm away, making it virtually impossible to fit all the mirrors and filters in. This essentially means a transillumination setup must be used.

Thankfully, we at least have one advantage over a traditional transillumination setup: we have darkfield. By setting up the fluorescence LED in the same orientation as the darkfield LED, we get a similar effect to epifluorescence in the sense that only scattered light can make it to the camera. Even still, the emission light must somehow be distinguishable from the excitation light in order to tell the difference between darkfield and fluorescence. For this, we tested three different possibilities:

- Detect the difference in color using the bayer filter
- Filter out the excitation with the phone's UV filter
- Use custom-sized interference filters

Spectral Unmixing with a Bayer Filter

Human eyes only have three distinct color sensors (cones) with peak sensitivities in red, green, and blue; yet we can generally make a solid guess at the wavelength of light we are sensing by looking at the combination of all three sensor intensities. This process is called spectral unmixing. The issue is that this is an inherently unsolvable problem, with different combinations of wavelengths being interpreted as the same color (these different combinations are called metamers). That is why screens, like the one you're probably reading this on, can appear to produce most of the visible spectrum of light despite only having red, green, and blue pixels.

Phone cameras work in basically the same way. The combination of the bayer filter and the inherent sensitivity curve of silicon creates three distinct color sensitivities (see figure 2.6). Three distinct sensitivities means we can definitely separate at least three different light source signals—assuming the camera signal from each source isn't hitting the noise floor or

saturating. So one of the three will be the excitation light, leaving two distinct emission profiles that can be computationally separated out.

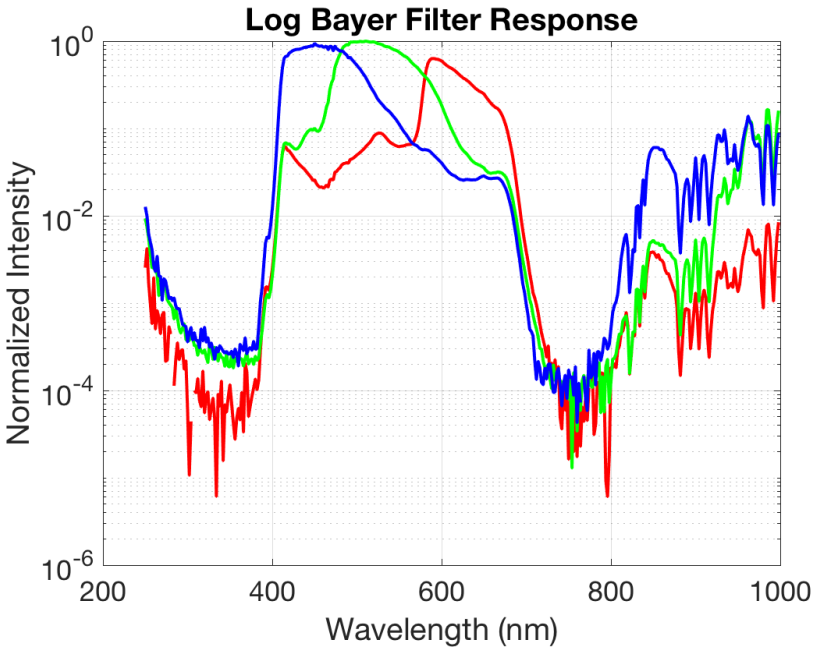

Figure 2.6: **Sample Sensitivity Curves of Bayer Filter.** Data collected by taking raw photos of a spectrophotometer light source with a Huawei Honor 9 Lite. The data was normalized with the provided intensity spectrum of the Xenon lamp. Noise in the infrared is likely due to a mismatch between the provided intensity spectrum and the actual intensity at wavelengths of known high-intensity peaks. Note: this phone does have a standard infrared filter.

Sadly, that assumption does not hold in practice. The scattered excitation light from a physiologically relevant fluorescent sample was still around three orders of magnitude brighter than the emission signal. Looking back at figure 2.6, even under ideal conditions, the bayer filter would only suppress the excitation light relative to the emission by around one order. Since the dynamic range of the sensor is approximately two orders, that means that preventing the excitation light from saturating the sensor also meant driving the emission light into the noise floor.

Fluorescence with a UV Filter

Luckily, there are two more filters built into most modern phone cameras: a UV filter (a frame of glass that protects the lens module) and an IR filter (a thin element located between the lens module and the sensor). The IR filter doesn't help much here since the idea is to be able to see light of a longer wavelength than the excitation light, but the UV filter does. Again

looking at figure 2.6, the UV filter causes a 3-order reduction in signal intensity between 380nm light and below vs 420nm and above.

The system was tested using a calcofluor white-stained sample, first using a 380nm LED, and then a 365nm LED. The 380nm LED's blue tail was still enough to drown out the image, but the 365 was enough that the fluorescent areas of the sample were clearly visible above the blue background. What this meant is that we had a system that could achieve fluorescence with no added filters (illuminated with the same setup as darkfield), but was limited to fluorophores that could be excited in the deep UV and still emit at least in the mid blues. The next section will delve deeper into how this system was used in the field.

Implementing a (Relatively) Standard Transillumination Setup

Before delving into the field implementation, there is one more setup worth mentioning: added filters. While interference filters are an expensive addition, they offer a potentially large performance boost. Running a UV LED or laser through a short-pass filter cuts off the blue tail and will drastically improve the signal to background ratio. Adding an emission filter between the two lenses would also allow for excitation wavelengths within the visible range (assuming a properly matched excitation filter). With modern bandpass and notch filters, the entire system can be left in solid state while maintaining almost full color sensitivity regardless of the excitation wavelength.

The cost of interference filters scales somewhat linearly with the area of the filter [61, 62]. By placing the excitation filter directly in front of the LED or laser, and the emission filter between the objective and camera lens, the area of each filter can be limited to less than 25 square millimeters. A suitable excitation/emission pair from Chroma costs a total of $475 where each filter is has a diameter of 25mm. Given the reduction in required area, combined with bulk pricing, it is easy to assume the total cost of the filters will be less than $25.

The advantage of using interference filters is that optical density can be tuned to be extremely high (over 6) over a very specific area, and using a very thin substrate (Chroma's standard is 1mm thick glass, but thicknesses below 0.5mm are possible–anything below that becomes extremely fragile). The main disadvantage is that their carefully specified absorption curve blue-shifts as the angle of light increases. Columnating the LED or using a laser keeps the excitation angle close to 0 degrees, but emission light through the non-telecentric setup cannot be constrained that way. No matter what, high angle light (40 or more degrees) will hit the filter. Since the fluorophores emit isotropically, placing the filter between the sample and the objective (and by the same token, between the camera lens and the sensor) will mean every point in the field of view is comprised of a large array of angles, effectively smoothing the absorption curve. The other possibility is to put the filter between the objective and camera lenses, where the angle of light is associated with the field angle–the angle of light will increase with distance from the center of the FOV. The advantage of the second setup is that even if the angle is sufficiently high to allow for overlap between

the excitation and emission filters, at least a part of the FOV (i.e. the center) will still be filtering the excitation light properly.

2.4 Example Implementation: Multi-Contrast Imaging of Fusarium Oxysporum

A few years ago, the Cloud-Based Intelligent Total Analysis System (CITAS) team based at the University of Ateneo de Manila University reached out to Fletcherlab to collaborate an a new diagnostics project. The goal was to create a portable diagnostic device that could detect Fusarium oxysporum f. sp. cubense (Foc); specifically tropical race 4 (TR4).

The story begins as early as the 1800's, when Fusarium was first discovered in Australia, Costa Rica, and Panama [63, 64]. From there, it continued to spread and is now found in almost every banana-producing country [65]. While the fungus is harmless to humans, it causes "Fusarium wilt" in banana plants, which slows growth and can kill the plant (see figure 2.7). This effect took a global stage when the main world banana export, the Gros Michel, succumbed to Foc tropical race 1, bringing it almost to extinction within a few decades [66].

The main issue is that the Gros Michel was a monocrop: every plant on Earth was essentially just a clone of one another. This meant that a disease that could kill one plant could kill them all. Efforts to create a Foc resistant crop failed, and the Foc TR1-resistant Cavendish banana took over as the globally exported banana–the large yellow banana we still see in grocery stores today [67, 68]. But while the Cavendish had filled in the gap left by the Gros Michel, it did nothing to alleviate the underlying issue: the main global banana export is still a monocrop.

That brings us to today, where Foc TR4 has become to the Cavendish what TR1 was to the Gros Michel. Despite efforts to limit spreading, TR4 is now found in northern Australia, much of southeast Asia, and more recently in Jordan and Mozambique [69–72]. With funding from The Philippine-California Advanced Research Institutes (PCARI) project, we partnered with the CITAS team to create a field diagnostic that could prevent the spread of Foc TR4 by detecting its existence in soil and plants as early as possible.

Diagnostic Methods

The main goal of the project is to be able to detect Foc TR4 in soil before plants are symptomatic, or even before plants are planted in the first place. While the technology already exists, the current workflow requires a soil sample to be sent to a lab for PCR analysis done by a trained expert. With many plantations being located far from such facilities, regular testing becomes impractical. With a portable device that can automatically detect the presence of fusarium on-site, the lab bandwidth (and cost) can be reserved for only the soil samples containing fusarium.

Figure 2.7: **Examples of Fusarium wilt in the Philippines.** *Top-left*: Dead banana plant infected with Foc TR4. *Top-right*: dying banana plant–the edge of the leaf has lost all circulation while the root is still alive. *Bottom*: an area of the same plantation where the soil is too heavily infected with Foc TR4 for any plants to grow. Photos were taken on my trip to the Philippines for the initial field trial of the scope.

Thus, the workflow was developed. Farmers are given a device to keep for regular testing of their fields and for testing of new soils before expanding their crop. The device has an onboard app that basically amounts to a "scan now" button. For each soil sample, farmers will use a pre-made kit to collect the sample, dilute it with water, and add a calcofluor white stain. The same capillaries used for the LoaScope can then be dipped into the solution (after a few minutes of settling), which will wick the sample into the imaging chamber. Finally, the capillary is inserted into the device for imaging.

While imaging, the device switches between brightfield, darkfield, and fluorescent illumination for each field of view in order to gather a multicontrast dataset. The rationale is that we are looking for the Foc chlamydospores and microconidia, both of which are mostly transparent–macrospores are usually only found in actual banana plants, not in soil. Thus, anything with high contrast in brightfield can be ruled out, and anything no contrast in fluorescence can also be ruled out (the calcofluor white stain binds to chitin, which is what the

fungal walls are mostly made of)[73]. This leaves the darkfield image for the highest contrast data, especially for small specimens like the microconidia. Darkfield on its own, however, would be difficult to use given that it highlights all particles, including suspended dust and soil. Preferentially scanning only the areas that have not been omitted by brightfield and fluorescence should drastically improve the false positive rate.

After image analysis is complete, the app informs the user as to whether or not the soil contains fusarium. The farmer can then decide if they should send the soil sample to a professional lab for further testing. The capillary itself can then be discarded as normal waste or saved for further manual analysis by a microscopist.

As a clarification, the above workflow is the final goal of the project. The automated algorithm has yet to be developed, and the devices have not yet been made in sufficient quantities to be able to be left with a farmer. The next sections go through a preliminary data collection trial done on-site in the Philippines.

A Quick Aside on On-Site Testing

Before showing the results of the field trial, I want to highlight exactly why we need this to be a *portable* diagnostic. We went to two banana plantations during my visit there (see figure 2.8 for photos). One was on the southern island of General Santos, which solidly fits into the "developing country" category. While the plantation itself was quite well organized, the roads to get there were narrow and cycled between asphalt and dirt, miles away from any other form of development other than the airport. Both cars and people had to run through pools of bleach upon entering and exiting, and we had to wear disposable knee-high plastic boots in order to prevent the spread of fusarium.

While I didn't manage to get an exact area of the plantation, it was easily the size of a small/medium sized commercial farm in the US. Consistently testing an area that big is a daunting enough task; keeping all your samples accounted for as you ship them out for testing at a facility tens or hundreds of miles away is difficult at best. But with the modified LoaScope (or PlantScope as we called this version of the device), we could just go to each plot, grab a few soil samples, walk back to the van parked at the edge of the plot, suspend them in water/stain, wick into capillaries, and image all the samples on the spot. Each plot took at most ten minutes to drive to, select areas for sampling, and test.

The second plantation was much smaller, but was an entirely different kind of challenge. Though it was less than 40km from Manila, it took us four hours of driving each way (first due to the world renowned Manila traffic, and then because of the endless winding roads traversing the jungle–the rain didn't help). Then came the 15 minute hike through dense jungle to reach the farmer's house. We set up the lab supplies on a table outside, then continued for a few more minutes into the jungle to get to the "plantation" – some ten or so giant banana plants spread out over a few acres of jungle dense enough to make us grateful for the machete the farmer gave us. Yet despite the long journey, the perpetual drizzle, and the dense landscape, we were able to sample all the plants and image the samples on site in the period of a half hour.

Figure 2.8: **Field Trial Working Conditions.** *Top-Left:* Bleach pool in driveway to sanitize incoming and outgoing traffic. Smaller versions were placed on adjacent walkways for foot traffic. *Top-Right:* Running an imaging scan on an infected plot at the General Santos location. *Bottom-Left:* Trekking through the main-island plantation to gather soil samples near the banana plants. *Bottom-Right:* The "testing area." A small space clear of plants next to the farmer's house.

For someone like that plantation's farmer, a device like the PlantScope quickly becomes the only viable option for consistent monitoring. While there is still a lot of work left to be done before the PlantScope images can be classified diagnostically, the field tests themselves revealed just how useful the test will be once it is refined and automated.

Results of Multi-Contrast Fusarium Imaging

Figure 2.9 shows an example multicontrast acquisition of an artificially infected soil sample (it is extremely difficult to tell if the actual field samples are infected without a computer vision algorithm–this sample is shown in order to demonstrate the potential benefits of multicontrast imaging). Looking at the fluorescence image, most of the short, narrow structures (like those shown in the orange circle) are microconidia, while the large granular structures are mostly clusters of chlamydospores.

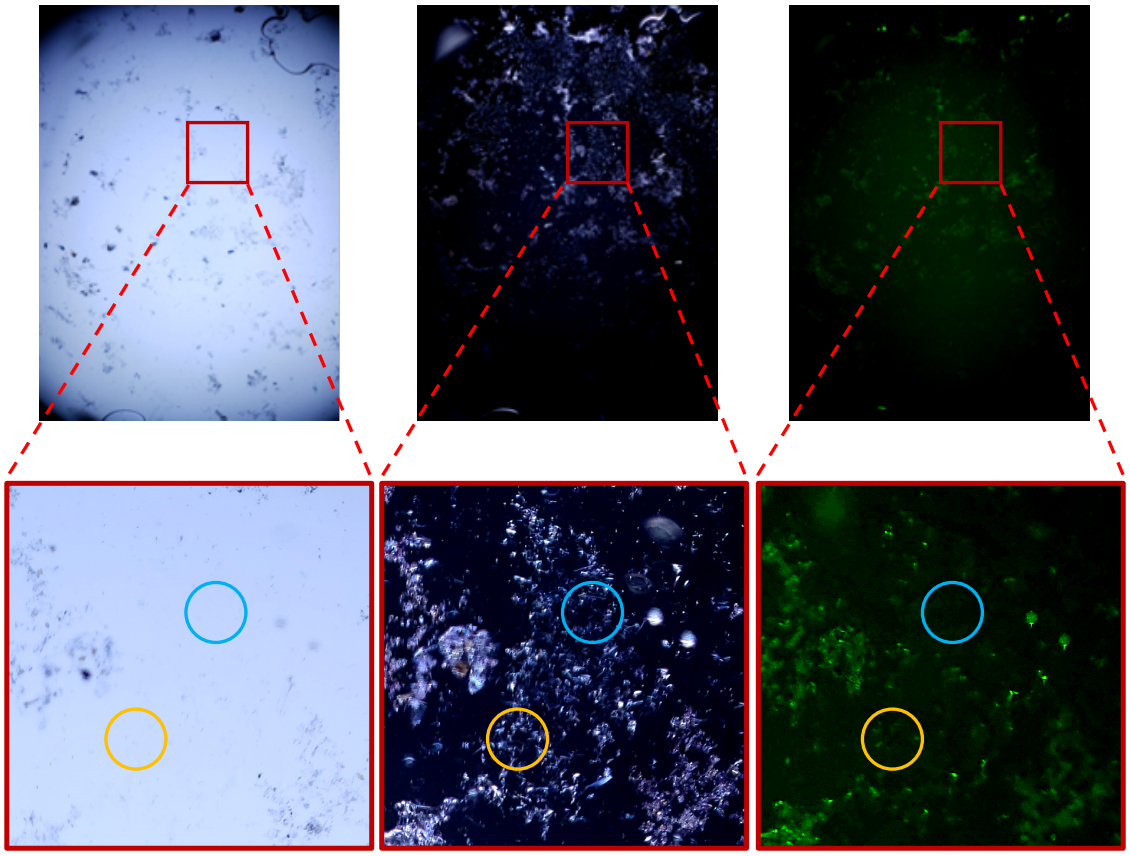

Figure 2.9: **Example multicontrast acquisition of Foc soil sample.** Contrast from left to right: brightfield, darkfield, fluorescence. Field of view of zoomed area is 800μm x 800μm. The blue circle shows a negative area of the sample, while the orange circle shows an area of the sample with three Foc microconidia. Note the lack of contrast in brightfield and the similarity in appearance in darkfield between the two areas. Photos taken with a Samsung Galaxy S9 with an ISO of 50, a 1ms exposure for brightfield, and a 200ms exposure for fluorescence and darkfield. Only green and red channels were used in the fluorescence image to reduce background from the blue tail of the 340nm LED.

At a first glance, it is easy to see that the microconidia have almost no contrast in brightfield. Also, while the chlamydospore clusters do show up, the contrast is too poor to make out individual spores. However, this also means that anything with higher contrast, such as the areas in figure 2.9 with large black structures can be ruled out right away. The vignetting in the image is mostly due to the gap between the reversed lens and the internal phone camera lens. It is impossible to shrink that gap enough without modifying the phone due to the protective window over the camera lens.

The darkfield image is by far the busiest of the three contrast modalities. It highlights small and sharp-edged objects, most of which are soil particles. By comparing it to the

fluorescence image, we can start to pick out the microconidia among the background of soil. Note that the dynamic range for the darkfield image is around 7 bits while the dynamic range for the fluorescence image is less than 5, so even if the morphology does show up in the fluorescence image, the darkfield image can still be very useful for coaxing out all the possible information out of the system.

2.5 Conclusions

Overall, the illumination implementations described in this chapter did provide three distinct contrast modalities that could potentially be used for diagnostic imaging. However, some improvements are required to maximize the utility of the system.

One issue to note is the lack of illumination uniformity in the darkfield and fluorescence images. As mentioned in the previous sections, this version of the scope illuminates the sample with high angle light from only one direction. While we were hoping this would be enough to illuminate the sample, the high density of soil absorbed enough light to darken a significant portion of the field of view. The next generation of devices will be designed with at least two opposing light sources to counteract this issue. However, as discussed in Chapter 3, an alternative illumination method is possible that can provide virtually uniform contrast–including phase contrast–across the field of view, regardless of sample density.

Another practical issue came up during this field trial: how do we train the computer vision algorithms on a dataset that we can't confidently label? While the biologists on the team can very accurately label datasets taken at very high resolution (such as on a 40x/.6NA objective-based microscope), the sampling-limited resolution of the PlantScope created images of the microconidia that were too pixelated to label with enough confidence. Thus, both for the purposes of labeling training sets, as well as potentially improving the accuracy of the classification algorithms, a higher-resolution version of the scope would be very useful. Chapter 4 discusses one potential avenue for improving resolution without added hardware.

Chapter 3

Multi-Contrast Microscopy on a Mobile Phone-Based Platform

Use of reversed mobile phone lenses [45] enables high-resolution imaging over extremely large fields of view, and their use has already enabled deployment of low cost diagnostics in low-resource areas [74]. The inherent processing power of smart phones makes this approach a natural fit for contrast enhancement via computational imaging methods [75–78]. Such enhancements would open the door for additional label-free diagnostic approaches, reducing sample preparation requirements and enhancing the information available for automated image recognition and machine-learning-based algorithms [79]. Differential phase contrast (DPC) and other computational imaging modalities typically depend on approximately telecentric imaging systems, limiting field of view to less than the lens area and restricting low-cost lens options. This chapter presents an approach for extending such techniques to highly nontelecentric systems, and demonstrate its efficacy in an extremely non-telecentric reversed lens system.

3.1 Background

A telecentric system is defined by having its entrance pupil at infinity with respect to the object; this is another way of stating that the field angles (also known as Chief Ray Angles, CRA) will be zero for every point in the field of view, and can be accomplished by locating the system aperture stop in the back focal plane of the objective lens. A telecentric system presents the same pupil to every point in the field of view (FOV), resulting (in an aberration-free system) in a space-invariant point-spread-function (PSF) and thus resolution. This is a desirable feature in quantitative microscopy, but also in terms of theoretical analysis since the space-invariance allows the usual superposition integral relating object and image fields to be replaced by a convolution, opening the door to Fourier analysis [80, 81]. So-called "4-F" afocal relay systems often cited in Fourier-optical treatments are typically intended to be telecentric, with the aperture stop placed in the back focal plane (BFP) of the objective

and front focal plane (FFP) of the tube lens respectively. From the standpoint of microscopy, object-side telecentricity also results in no change in apparent magnification with defocus or object tilt [82], and simplifies any corrections for coverslip thickness (e.g. via correction collars), making it additionally desirable in, and a usual feature of, a microscope objectives.

Telecentric systems have the known disadvantage that the objective lens must be at least as large as the object field to be imaged (based on simple geometry, the limitation is actually that the lens diameter must be at least the $d = FOV_{dia} + 2WD \times NA$, where WD is the working distance of the lens and we have approximated $tan\theta \approx sin\theta$; the limitation is thus more pronounced for high NA systems). Since for diagnostics based on detecting presence of a pathogen Poisson statistics give an exponential increase in diagnostic sensitivity with field of view examined [45], the limitation on FOV due to lens size is particularly disadvantageous. Beyond this, the simple size and cost of larger lens systems makes them less likely to be manufactured in the extremely high quantities that result in affordable high performance. For instance, it is only the manufacturing volumes in the 10's to 100's of millions that enable cellphone lenses that cost $<$ \$10 each yet provide nearly diffraction limited performance across a $\approx 36^o$ half-angular FOV due to tight assembly tolerances and 10 separate highly aspheric surfaces [47]. Systems built using single-lens van Leeuwenhoek geometries cannot provide anything approaching diagnostically significant fields of view, limiting any medical import of their potential high resolution; in fact, such systems are approximately telecentric (though without benefit of large FOV) because their extremely high field curvature limits in any useable image to small FOV radii and thus small CRA's.

Approaches to enhancing imaging contrast – notably extending it to phase objects – have existed for many years. However, the advent of digital computing and imaging have led to a recent emergence of new techniques which use multiple images of differing illumination conditions and subsequent computational processing to provide differential phase contrast (DPC), and in a number of approaches recover full quantitative information about both the amplitude and phase (e.g. Quantitative DPC (QDPC) and Fourier ptychography (FP)) of the imaged object function [75, 76, 78, 83–85].

DPC, and its relative QDPC (Quantitiative DPC) are typically efficient, since image reconstruction is based on a small number of images (as few as two or four [78]); in contrast, FP requires a large number of images, often each requiring long exposures due to illumination etendue limitations imposed by the requirement for reasonably large illumination coherence areas at the sample, and each requiring multiple computational steps for iterative phase retrieval [75]. Although FP offers the possibility of enhanced resolution, as well as full information about the object function, these disadvantages currently limit its utility for low-cost, point-of-care (POC) diagnostic use. Thus we have focused on DPC and QDPC as an approach to providing additional sample information in a low-cost and computationally efficient way.

Non-Telecentric Imaging

The reversed-lens configuration is highly non-telecentric, with chief ray angles (field angles) for collection potentially range up to 36 [45, 47]. For simplicity of analysis, we will approximate the system as a simple, aberration-free lens (see figure 3.1).

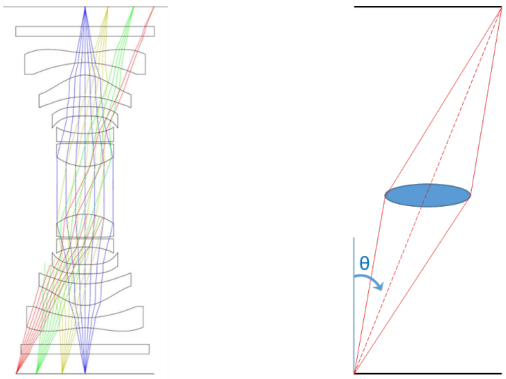

Figure 3.1: **Simplified model of the reversed lens system.** Reversed-mobile-phone lenses (left) [45] modeled as a single thin lens (right) with defined diameter d and field angle (CRA) θ. Thin lens is aberration-free (hence no field curvature). As is evident in the red rays traced in the reversed lens configuration, there is no single aperture stop limiting the light path; as discussed in the text, the aperture in the reversed-lens configuration is not cleanly defined. In the actual device, $|\theta| \approx 36^o$.

After approximating the system as a single-lens imaging system, the collection angles become geometrically straightforward (see figure 3.1). Assuming a lens (i.e., entrance pupil) of radius r_{pupil}, object distance so, and field radius r_{field}, the collection angles become:

$$tan(\theta_{CRA}) = \frac{r_{field}}{s_o}$$
$$tan(\theta_{max}) = \frac{r_{field} + r_{pupil}}{s_o}$$
$$tan(\theta_{min}) = \frac{r_{field} - r_{pupil}}{s_o}$$
$$tan(\phi) = \frac{\sqrt{r_{field}^2 + r_{pupil}^2}}{s_o}$$

where θ_{CRA}, θ_{max}, θ_{min}, and ϕ represent the central tangential field angle, maximum tangential field angle, minimum tangential field angle, and sagittal field half-angle respectively.

A consequence of this imaging geometry is that illumination from a given angle may fall inside the collection NA (see figure 3.1) for some field positions, resulting in brightfield contrast (see figure 3.1), and outside the collection NA for other sample positions, resulting

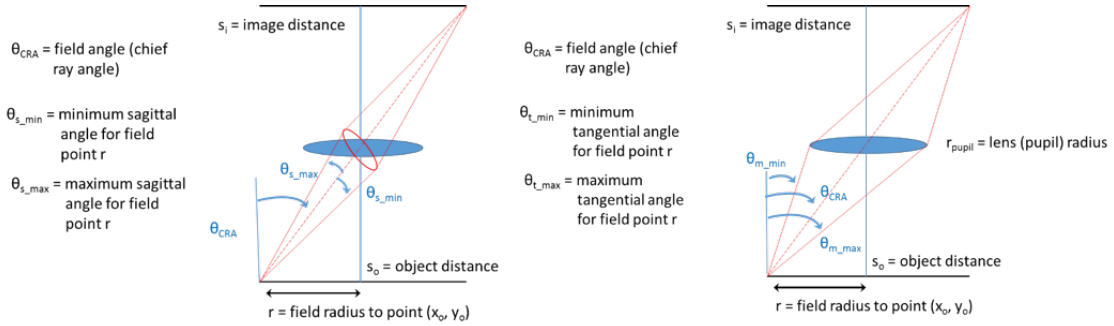

Figure 3.2: **Variability of collection NA across field of view.** Collection NA (angles) for a field point imaged by a single thin lens. Off-axis pupil presents an elliptical entrance pupil (and hence frequency-space bandpass) to the sample point. Any illumination falling within this acceptance angles will result in brightfield illumination at the corresponding image point.

in darkfield contrast. This complicates implementation of illumination for all contrasts; any light providing illumination concentrated along the optic axis (e.g. a LED, flashlight, or even a traditional condenser) will illuminate only the center of the FOV in brightfield, resulting in highly vignetted illumination and failure of computationally generated images such as those from DPC (see figure 3.4). Solutions for this involve diffusers and/or multiple imaging sources (e.g. a domed LED array [77]) which serve to provide illumination at a range of angles at least some of which fall inside the collection NA for every point in the FOV.

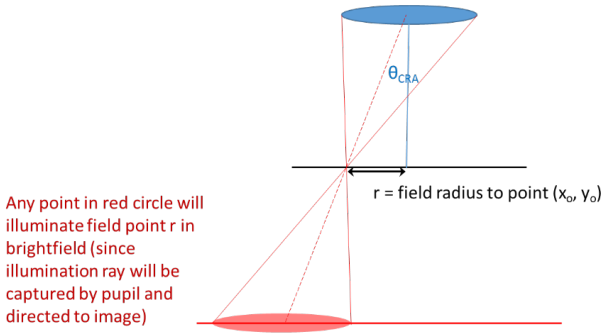

Figure 3.3: **Geometry of brightfield illumination.** Illumination field area (red) which will result in brightfield contrast for a field point at radius r, with light collected and imaged by a single thin lens (in blue).

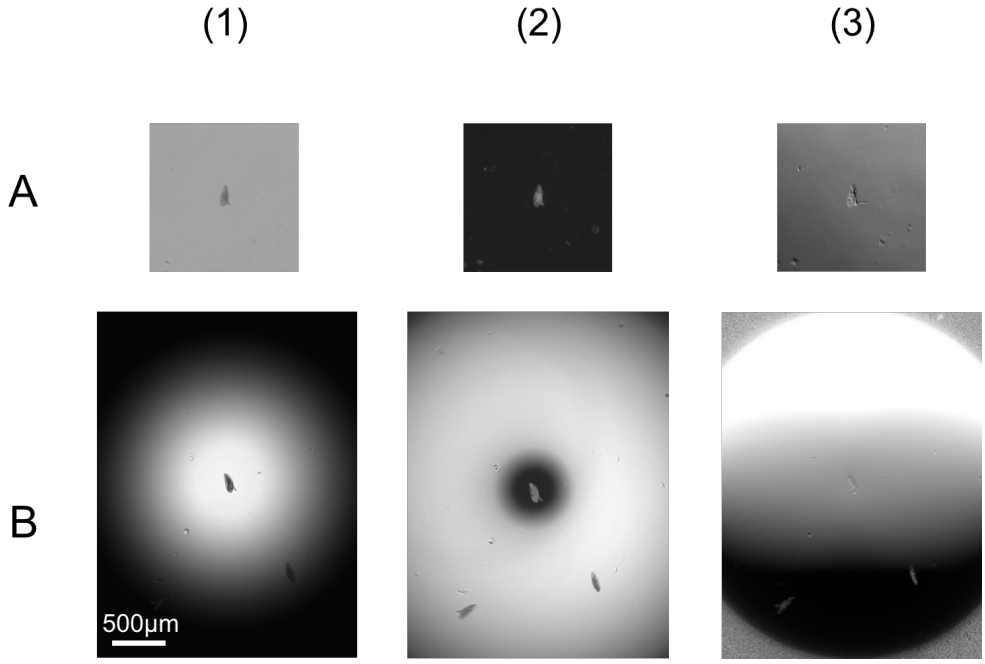

Figure 3.4: **Comparison of contrast modalities using telecentric and non-telecentric systems.** Microscopy of unstained schistosoma eggs under standard illumination with a telecentric (A) and non-telecentric (B) system. Columns (1), (2), and (3), show brightfield, darkfield, and DPC images respectively. Identical illumination was used for the telecentric and non-telecentric case. Note that the scale in all images is the same, but the the non-telecentric images were cropped to 50% of the full size image to avoid making the features too small.

3.2 Understanding the Fundamentals of DPC

Before delving into possible solutions for the contrast non-uniformity, I want to take a moment to outline a simplified mathematical basis for how DPC works. The entire example below is for a 1D case, but can be generalized for 2D. Note that this explanation assumes the reader has a reasonable understanding of Abbe theory and Fourier transforms.

Let's begin with the general case: we transilluminate a sample with light intensity $I(\theta)$– as in we are specifying the intensity of light hitting the sample from any particular angle. The sample will both absorb the light and change the phase delay of the light with respect to light that did not shine through the sample. This can be expressed by the function:

$$O(x) = e^{-\mu(x)} \cdot e^{i\phi(x)}$$

Where $\mu(x)$ is the optical absorption coefficient and $\phi(x)$ is the phase delay coefficient. We can then measure the amplitude and phase directly after the sample as:

$$S(x) = I(\theta) \cdot O(x)$$

Now let's simplify the setup and probe the system to see what happens. Let's assume the sample does not absorb light ($\mu = 0$) and has a very small phase delay ($\phi << 2\pi$). We can use the Taylor expansion of S(x) to simplify:

$$S(x) = e^{i\phi(x)} \approx 1 + i\phi(x) + \cancel{H.O.T.}$$

where we remove higher order terms ($H.O.T.$). Since there is a 1 in that equation (i.e. the brightfield background) and we are assuming $\phi(x) << 1$, we can assume any term with an exponent greater than 1 over $\phi(x)$ can be assumed to be 0. We are also implicitly assuming that the angles of light hitting the sample are within the collection cone of the objective and that illumination is symmetrical, as is the case for normal brightfield.

When the light hits the sensor (either your eye or the camera), it is the light *intensity*, not amplitude that is recorded (intensity is the square of magnitude of amplitude). Thus our final recorded image is recorded as:

$$|S|^2 = (1 + i\phi(x))^2 = 1 + \cancel{\phi^2(x)}$$

Again, we can assume that the $\phi(x)$ term is essentially equal to 0 because of the square. This means our entire image has a recorded intensity value of 1. Since contrast is a function of the difference between the maximum and minimum value of the image, the recorded image has no contrast. This is why brightfield illumination usually cannot be used to visualize clear objects, such as unstained cheek epithelial cells.

But what happens if the illumination is not symmetric? Let's take the case where our sample does not absorb light, but varies sinusoidally in phase with amplitude α and frequency k_0:

$$O(x) = e^{i\alpha sin(2\pi i k_0 x)}$$

Where $\alpha << 1$. Furthermore, we will illuminate with exactly one angle of light: $\theta = C$. This effectively shifts the image in the back focal plane (BFP) of the objective, which also causes a shift in the Fourier spectrum of the image. According to shift theorem, this multiplies the x-space image by $e^{2\pi i k_i x}$ where k_i is the spatial frequency associated with the Fourier shift. This leaves us with:

$$S \approx e^{2\pi i k_i x} \cdot (1 + i\alpha sin(2\pi i k_0 x))$$

Back in the Fourier domain, this translates to:

$$\overline{S} = \delta(k - k_i) + \frac{i\alpha}{2i}[\delta(k + k_i + k_0) - \delta(k - k_i - k_0)]$$

Now here is where the magic begins–the objective aperture acts as a band-pass filter from $-k_{NA}$ to $+k_{NA}$ where k_{NA} equals the ratio NA of the objective and the wavelength of the

illumination light. But with the added shift from the off-axis illumination, that bandpass range shifts by k_i. What if we choose C such that $k_i + k_0 > k_{NA}$? Looking back to the above equation, that would mean that the last term would not pass through the bandpass filter, leaving us with:

$$\overline{S_+} = \delta(k - k_i) + \frac{\alpha}{2}\delta(k + k_i + k_0)$$

Where S_+ denotes that the bandpass filter has been shifted sufficiently to block the negative delta term. Back in x-space, we're left with:

$$S_+ = e^{2\pi i k_i x} + \frac{\alpha}{2}e^{2\pi i(k_i+k_0)x} = e^{2\pi i k_i x}(1 + \frac{\alpha}{2}e^{2\pi i k_0 x})$$

Collecting the light at the sensor, we get an intensity of:

$$|S_+|^2 = 1^2 + \frac{\alpha}{2}e^{2\pi i k_0 x} + \frac{\alpha}{2}e^{-2\pi i k_0 x} + \cancel{\frac{\alpha^2}{4}}$$

Using the cosine identity, we can simplify to:

$$|S_+|^2 = 1 + \alpha cos(2\pi k_0 x)$$

Notice that we're left with a weak but detectible sinusoidal signal, just 90 degrees shifted. We can also take a second image with the opposite illumination angle to get:

$$|S_-|^2 = 1 - \alpha cos(2\pi k_0 x)$$

Finally, by taking the difference between the two images and dividing the result by the sum of the images (i.e. the brightfield image), we get:

$$DPC = \frac{|S_+|^2 - |S_-|^2}{|S_+|^2 + |S_-|^2} = \alpha cos(2\pi k_0 x)$$

Notice that we're now left with a sinusoid that, while phase shifted by 90 degrees, has the same amplitude and spatial frequency as the original phase function. We've successfully translated phase delay into intensity.

Going back to the subject of this chapter, the issue with this proof is we implicitly assumed that the back focal plane was the Fourier transform of the image when illuminated by one angle. While basically true for a telecentric setup, it is absolutely not the case in a non-telecentric system.

3.3 Approach: A patch illumination solution to multi-contrast non-telecentric imaging

One solution is a patch-based illumination system where the field of view (FOV) is segmented into small circular segments that can be assumed to be isoplanetic (pupil does not appreciably

change) from one side to the other. To calculate the size and location of these patches, we begin by mapping the minimum and maximum illumination angle that can be seen for each pixel in the field of view (see figure 3.5). From there, the following protocol is used:

A pixel in the FOV is chosen to act as the left-most point in the patch (how to choose this pixel becomes clear at the end of the protocol). Then, an illumination angle is found that corresponds with the maximum acceptance angle for that pixel. The minimum acceptance angle is then calculated as $\theta_{min} = \theta_{max} - 2sin^{-1}(NA_{pupil}\alpha)$ where α is a predetermined value equal to $1 - (NA_{illum}/NA_{pupil})$, θ_{max} is the maximum illumination angle found in the previous step, NA_{pupil} is the numerical aperture of the local pupil, and NA_{illum} is the numerical aperture of the local illumination. A second pixel is then selected by finding the right-most pixel that still accepts the above illumination angle. The pixel between the two above pixels is then assumed to be the center of the patch.

The vertical coordinates of the patch are calculated in a similar fashion. First, the minimum and maximum vertical illumination angles for the center pixel are found, and the average of the two is assumed to be the vertical center illumination angle (or field angle) of that pixel. The top and bottom illumination angles can then be calculated as $\theta_{max/min} = \theta_{center} \pm sin^{-1}(NA_{pupil}\alpha)$. The respective top and bottom pixels of the patch are found by finding the highest and lowest pixels that remain in brightfield from the above vertical angles.

Based on the four edge pixels found, an elliptical patch can be generated in the field of view. The same can be done in angle space with the four edge illumination angles. The entire process is then repeated where the rightmost pixel of the current ellipse becomes the leftmost pixel of the new ellipse. When a row has been filled, the same process is followed in the vertical direction to create a grid of patches.

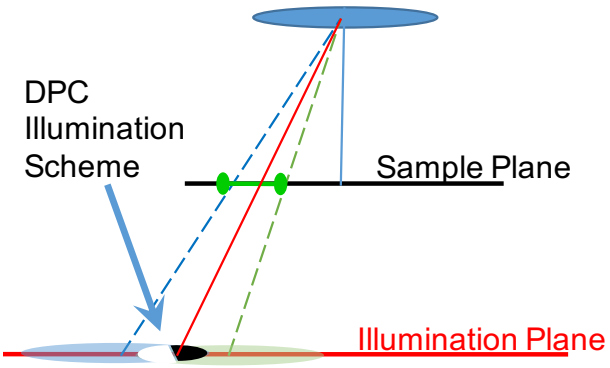

Figure 3.5: **Calculation of patch geometry.** Diagram for determining the location and dimensions of a single patch.

At this point, it is worth noting that, both from a geometrical perspective and from empirical data, it is safe to assume that the sample patches in the field of view are all equally sized perfect circles so long as the imaging system is largely distortion-free (i.e. max

distortion less than 1%). This assumption greatly simplifies the problem of packing the sample patches in an efficient manner as to cover the entire field of view. The radius of these circles is calculated from the patch that is centered directly in the middle of the FOV. This will be the assumption for all data shown from this point on.

Multiplexed Imaging

The number of images required to successfully illuminate the entire FOV can be drastically reduced by illuminating multiple patches at once. However, two key assumptions need to be made in order to do so: darkfield contributions must be negligible and illumination from one patch can not be within the brightfield cone of another simultaneous patch (see figure 3.6).

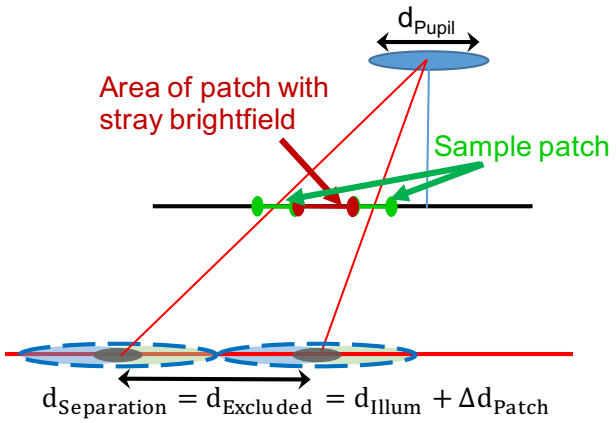

Figure 3.6: **Calculation of multiplexed patch geometry.** Diagram for determining the location of multiple patches within one frame in order to reduce overall acquisition time.

The first must be assumed because any area that is illuminated within the FOV will be picked up at all other areas in the FOV as either brightfield or darkfield (though the farther away the brightfield location is to another area, the smaller the darkfield contribution is in that area). The second assumption is necessary in order to hold the tightly-controlled illumination asymmetry necessary for the DPC algorithm to generate phase contrast. Thus, we have constraints on the tightest possible packing of patches, and therefore the maximum number of multiplexed patches per image.

Conversely, these constraints allow for a calculation of the lower bound to the number of images required to synthesize a full FOV image: the ratio of total space illuminated in brightfield due to a particular patch to the actual useable patch space is also the number of photos that must be taken if there is zero patch overlap. Of course, in practice, patches will always overlap (given their circular shape), meaning this lower bound is theoretical in nature, yet generalizable to any patch geometry.

Ensuring that darkfield contributions within a patch are excluded requires that the highest angle of illumination on one side of the patch is still less than the maximum acceptance angle at the point in the FOV corresponding to the opposing edge of the patch:

$$\theta_{illumination} = \theta_{pupil} - \theta_{CRA}$$

where $\theta_{illumination}$ represents the maximum illumination angle relative to a CRA of 0 degrees and θ_{pupil} represents the maximum acceptance angle of the pupil (for simplicity of the calculation, the pupil is assumed to stay constant in size throughout the field of view).

With the geometric argument of:

$$\theta_{CRA} = tan^{-1}\left(\frac{r}{f}\right)$$

where r is the radius from the center of the FOV and f is the focal length of the objective, we can calculate the maximum patch size for a given illumination angle:

$$r_{patch} = f \cdot tan(\theta_{pupil} - \theta_{illumination})$$

Similarly, the maximum radius of brightfield illuminated area can be calculated as:

$$r_{bf} = f \cdot tan(\theta_{pupil} + \theta_{illumination})$$

Thus the ratio of dead space to useful patch space can be calculated as:

$$R = \frac{\pi r_{bf}^2}{\pi r_{patch}^2} = \left(\frac{tan(\theta_{pupil} + \theta_{illumination})}{tan(\theta_{pupil} - \theta_{illumination})}\right)^2$$

Relating back to α, the small angle approximation allows for the simplified relationship:

$$\theta_{illumination} = (1 - \alpha)\theta_{pupil}$$

such that

$$\begin{aligned} r_{patch} &\approx f(\theta_{pupil} - \theta_{illumination}) \\ &= f(\theta_{pupil} - (1 - \alpha)\theta_{pupil}) \\ &= f\alpha\theta_{pupil} \\ r_{bf} &\approx f(2 - \alpha)\theta_{pupil} \end{aligned}$$

leaving the ratio, and thus the minimum number of images required as:

$$R \approx \left(\frac{2 - \alpha}{\alpha}\right)^2$$

Note that as α approaches small values, the number of images required increases dramatically.

Processing for Differential Phase Contrast

When image acquisition is complete, each sample patch will have two corresponding photos– a left- and a right- illuminated image. In the case of multiplexed images, the two photos will apply to all corresponding patches simultaneously. These pairs are then processed into single DPC phase images with the following formula:

$$DPC = \frac{I_1 - I_2 T}{I_1 + I_2 T}$$

where I_l is one of the two images in a pair, I_2 is the other of the two images, and T is a calibration transform to account for intensity variation across the patch. To calculate this transform, a one-time collection of blank images–using the same illumination patterns–must be taken. Then the transform can be calculated as $T = C_1/C_2$ where C_1 is one of the two calibration images in a pair (corresponding to the same illumination pattern as I_1), and C_2 is the other of the two images.

Once a DPC image is formed, the data within the appropriate patch areas can be added to a final combined image of all the patches. If patches overlap, the data in the final image is averaged between the overlapping datasets.

Experimental Setup

In order to speed the development process, the algorithm code was developed in MATLAB instead of directly on a smartphone platform, and was implemented by controlling both the illumination (an iPad mini retina screen) and camera (a raspberry pi cam 2.0 controlled by a raspberry pi 3.0) simultaneously from the MATLAB computer (see figure 3.7). To remain as close as possible to previously implemented smartphone-based microscopy systems and to minimize aberrations [39], the objective used was also a raspberry pi cam 2.0 lens. Thus, this system can be easily translated back to a portable system by bringing the computational processing and control back onto a smartphone platform and using the appropriate lenses.

The iPad screen was chosen as the illumination source due to its extremely high density of pixels, which could be used to very precisely control illumination angles on the sample. As will be discussed later on, this precise illumination control is crucial for the success of the patch illumination process. While a smaller screen such as a phone screen also has the requisite pixel density and can likely be used in a similar fashion, the large screen on the iPad also meant it could be positioned farther from the sample, allowing for the assumption that position on the screen corresponds to angle of illumination.

It is worth noting here that these camera/lens combinations are designed by the manufacturers to undersample the image in order to increase light sensitivity and/or size of the field of view. While this will cause aliasing in our system's images, we leave this problem to future work (Chapter 4 provides one possible solution to this issue) and focus specifically on characterizing effects that result from the optical illumination and collection.

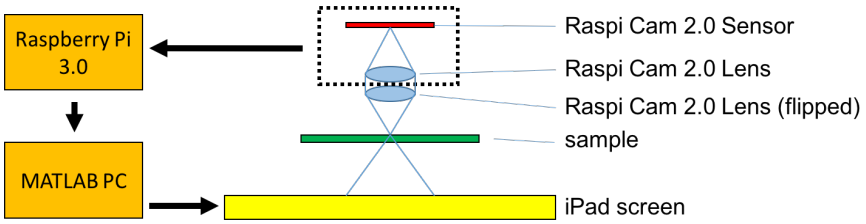

Figure 3.7: **Experimental setup.** The camera and camera lens are stock raspberry pi cameras (v2.0) and the objective is another raspberry pi cam 2.0 camera lens. Samples were placed on a z-adjustable stage and illuminated by an iPad mini placed 46mm below. The retina display on the iPad was controlled by a MATLAB script using the Duet Display app, providing an illumination angle resolution of $\leq .06°$. A Raspberry Pi Cam 2.0 lens is positioned in an inverted position over the sample to act as an objective lens, and the light is subsequently sent through a stock Raspberry Pi Cam 2.0 module (dotted box). The raw image data is collected and sent back to the main computer for MATLAB to process and interpret.

3.4 Experimental Results

Figures 3.8 and 3.9 show the final output of the above illumination algorithm. Using the images taken for DPC, all three contrast methods can be recovered to be mostly uniform across the field of view. Brightfield was constructed by adding the left and right images together instead of subtracting (while it is possible to simply add all the information together into one image, using only the patch areas increases contrast by removing darkfield contributions and/or creating a potentially more optimal modulation transfer function–this lends itself well to choosing an α value of 0.3). Darkfield was constructed by adding all the non-brightfield areas of each image together and normalizing for how many datapoints were added to any particular pixel. While the results in figure 3.8 appear normal at a first glance, a closer inspection of the non-idealities of the patch illumination is necessary to understand the minimal artifacts that remain.

3.5 Characterization of Effects of Illumination Asymmetry

Due to the patch nature of the system, tradeoffs between even k-space sampling and acquisition speed arise. At one end, an infinitely small patch size will allow the system to use identical illumination patterns to those used in a telecentric setup; however, this system will also require too many images to be taken to be feasible in practice.

At the other extreme, the patch size could be set to be as wide as possible without breaking the geometrical constraints listed above in order to dramatically cut down on the number

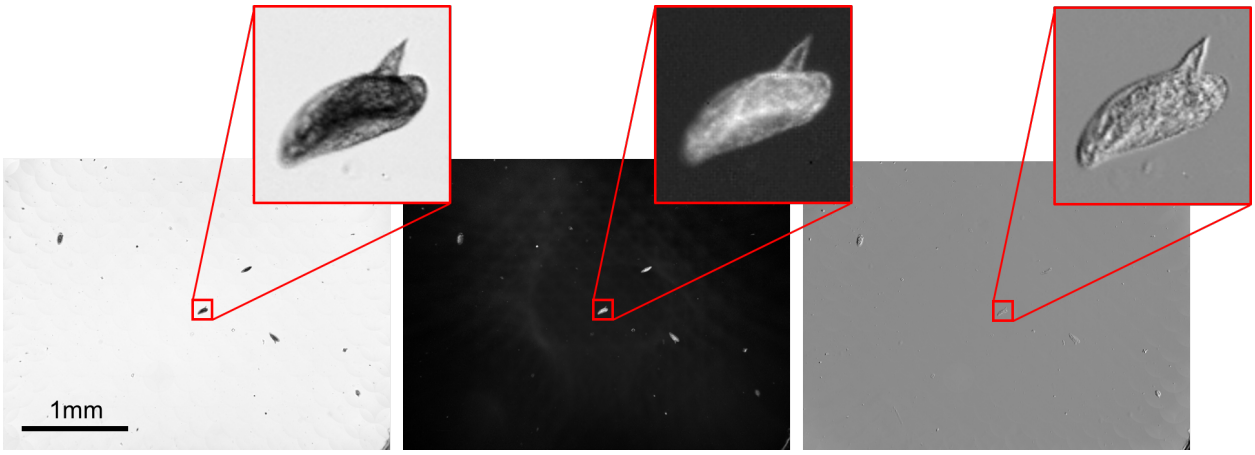

Figure 3.8: **Experimental result: simultaneous multicontrast illumination of unstained schistosoma eggs prepared on a glass slide.** Images from left to right with corresponding blowup views ($160\mu m$ FOV): brightfield, darkfield, DPC. Images were resized via bicubic interpolation for easier viewing of zoomed-in views. Images taken with patch sizes associated with an illumination fill of 70%.

of images necessary per acquisition. Here, however, the illumination NA will approach 0, drastically limiting the amount of light entering the system (at least with this current setup) and thus increasing exposure time to unreasonable levels. This will also halve the potential system resolution and introduce unwanted coherence effects. Furthermore, an underlying assumption of the system is that every pixel within the patch is illuminated symmetrically from either side (just in separate photos). This assumption breaks down as the edge of the patch becomes increasingly farther from the center. Finally, using an illumination NA below the NA of the objective spatially high-pass filters the data.

The above illumination asymmetry and high-pass filter effects are characterized in figure 3.10. To decouple the illumination effects from aberration effects, and to circumvent the necessity for multiple pure-phase sinusoidal gradings, all results were done in a custom MATLAB optical simulator.

The simulator emulates a sinusoidal phase grading with a "sample" input function of

$$f(x,y) = T \cdot e^{d(sin(2\pi kx)+.5)i}$$

where T, k, and d represent transmittance (set to 1 for pure phase), spatial frequency, and phase delay respectively. With this input, running different k-values through the simulator allows for an exploration of the spatial frequency response of the system. The simulator also takes an illumination input function, where each pixel in the 2D function corresponds to an illumination angle that will hit the sample (and the value of the pixel thus corresponding to the illumination amplitude at that angle of illumination).

The simulator processes the two input functions into an output image via the following

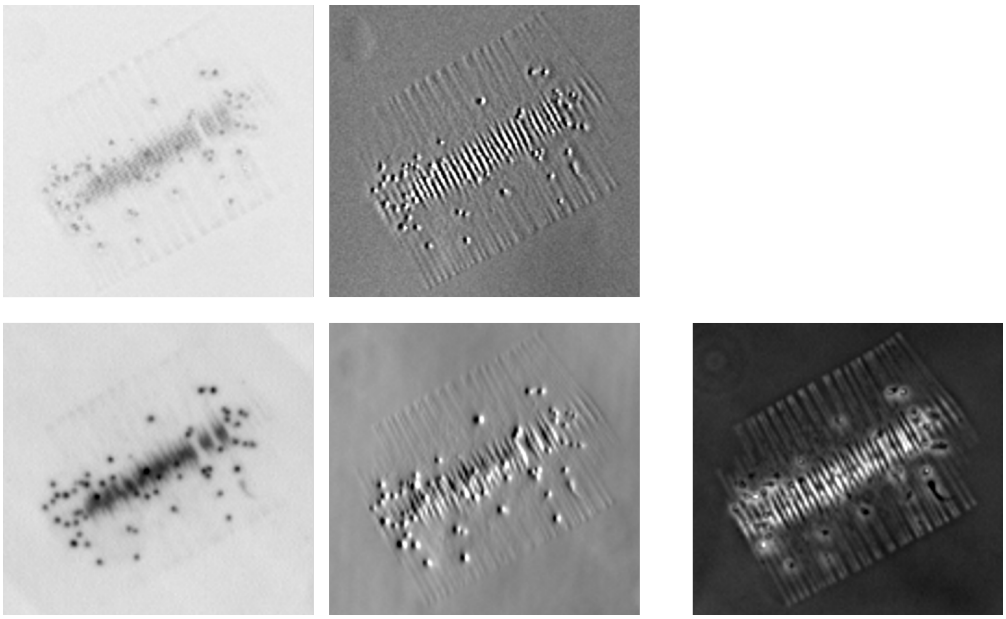

Figure 3.9: **Secondary result: Brightfield (left) and DPC (center) images of a plankton skeleton.** FOV = 190μm by 175μm. Images in the top row were taken at the center of the field of view of the non-telecentric system (illumination fill of 70%), while images in the bottom row were taken using the telecentric setup. Brightfield and DPC images were contrast stretched by the same amount to preserve differences in contrast in phase-only features. Phase image (right) was taken using a Ph1 objective as a pseudo-ground truth image. Note the difference in contrast of the features on the branches of the skeleton.

calculation:

$$O(x,y) = \sum_{n=-A/2}^{A/2} \sum_{m=-A/2}^{A/2} |\mathcal{F}^{-1}\{I(m,n)\mathcal{F}\{f(x,y)\} \cdot \psi\}|^2$$

where

$$\psi = circ\{x - g(m), y - g(n)\}$$

A is both the horizontal and vertical size of the image and must be a multiple of 2. The function $g(n)$ represents a coordinates transform to convert position in the illumination function, $I(m,n)$, into an x,y shift in the k-space filter ψ. Note that origin coordinates in this equation correspond to (A/2+1,A/2+1) to match with the MATLAB Fourier transform function. From there, the output could be treated as normal image data and the DPC algorithm could be conducted on a set of two images. Since the DPC algorithm produces values between 1 and -1, the image is transformed via $V(x,y) = U(x,y)/2 + 0.5$ to convert it to a standard 0-to-1-valued image. Finally, to avoid effects from edge artifacts, the image contrast is calculated using only the middle third of the image.

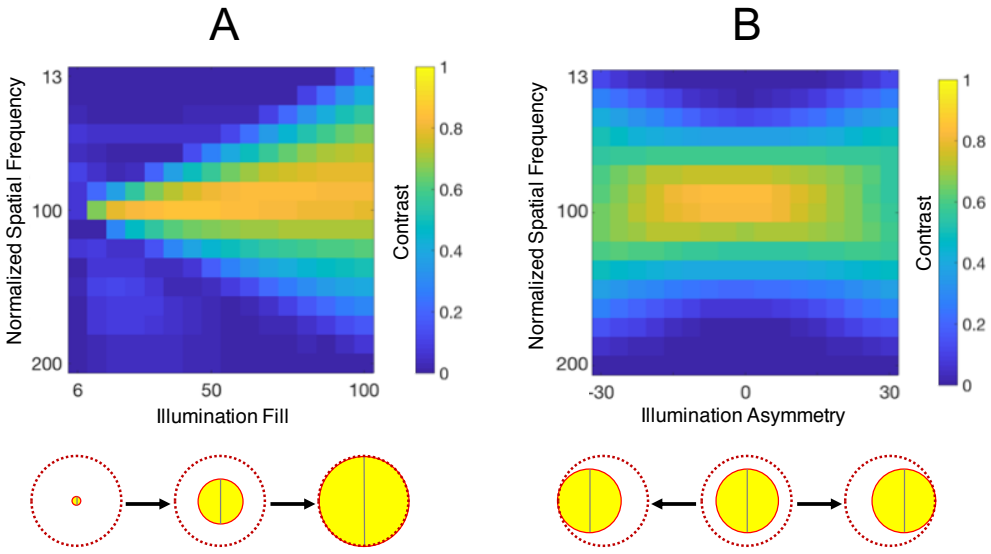

Figure 3.10: **Characterization of system non-idealities.** (A) MTF vs illumination fill, where the fill is defined as the ratio of illumination NA to the objective NA. (B) MTF vs illumination asymmetry, where asymmetry is defined as the ratio of the NA at the center of illumination to the objective NA. An illumination NA of $0.7NA_{objective}$ and its corresponding patch diameter were used. Spatial frequency was normalized such that a value of 100 equates to maximum spatial frequency allowed through a pupil with a given NA for a given wavelength of light at a 0 degree angle of incidence. Contrast was measured using a simulator emulating various sinusoidal phase gratings with 0.08 radian maximum phase delay.

The first experiment was designed to measure the contrast effects from varying the illumination NA. With the resolution target in the proper location in the FOV, the illumination NA was varied between 6% and 100% of the objective NA in 1/16 increments and DPC images were acquired for each illumination NA. This process was repeated for sinusoidal gradings of normalized spatial frequency 0.125 to 2 in increments of 1/8. The value is normalized to be a ratio of the spatial frequency in the image and the maximum spatial frequency collected by the objective of a specific NA at a specific wavelength with on-axis illumination.

The second experiment was designed to measure the contrast effects from an improperly-centered illumination shear axis, as would be the case for off-center areas of a patch. An illumination NA of $0.7NA_{objective}$ was used as a compromise between spatial bandwidth and the ability to shift the illumination off-center without introducing darkfield effects. The illumination patch was shifted from -30% to positive 30% in increments of 3.6% for the same spatial frequency range as above.

While many other factors, especially optical aberrations, will influence these results, the goal of this exercise was to characterize the two intrinsic and unavoidable non-idealities of the patch-based illumination scheme.

Characterization Experiments: Analysis

The illumination fill data in figure 3.10 matches with theoretical expectations: the lower the ratio between illumination NA and objective NA, the more overlap in spacial frequency sampling there would be from one image to another, resulting in a stronger high-pass effect on the spatial frequency response. At the same time, the lower the illumination NA, the lower the diffraction limit of the system becomes, decreasing the maximum spatial frequencies allowed through the simulated optical track. Both result in a predictable linear decrease in performance as patch size is increased.

The illumination asymmetry data is more difficult to interpret. At a first glance, it appears that illuminating off-center creates a scenario where overall contrast is reduced, but spatial bandwidth is improved. One must be cautious interpreting these results, however, as contrast alone does not fully describe the effects of asymmetry. As asymmetry is increased, so is an imbalance in contrast between positive- and negative-valued features. For instance, in the sinusoidal images used for this dataset, the output of highly-asymmetric images showed the wave thinning toward the minima and widening toward the maxima (or vice versa for asymmetry in the other direction). A quick Fourier-domain analysis shows that this is due to the increasing presence of higher evenly-spaced harmonics being introduced into the image.

Acquisition Time

One important point to note is that the time to acquire a full-FOV image can be significant given the low light levels of the screen illumination setup. Given the packing arrangement and α of 0.3 used for the figures in this chapter, 76 images were required at an exposure time of 2 seconds per image, meaning the total acquisition time was 152s. While potentially reasonable for diagnostic applications, this modality's usefulness is likely limited to still images. This could change by using a brighter (yet still pixel-dense) illumination source, such as with a fiber bundle, lensed LED array, or DLP projection arrangement.

3.6 Conclusions

The patch illumination technique allows for uniform multi-contrast illumination across the large field of view in a highly non-telecentric microscope, thus drastically increasing the range of samples and parasites that can be examined with minimal sample preparation under a non-telecentric microscopy platform. While the patch illumination does introduce artifacts into the system that would not be present in a telecentric system, the overall image quality is still more than adequate for a large range of point-of-care diagnostics.

Discussion

One unresolved issue with this method is the side effect of having a rotating shear axis across the FOV. As mentioned before, the pupil becomes increasingly elliptical toward the edge of

the FOV. Areas that do not fall directly on the x- or y- axis of the image no longer remain parallel to the axes, but instead rotate such that the minor axis of the ellipse points toward the optical center of the image (CRA equals 0). Ideally, the left and right images for each patch should shear across the minor axis, but that would lead significant non-uniformity in contrast across the FOV.

One possible solution is to adapt the patch illumination method to a quantitative DPC algorithm. By taking four images at each patch (one set aligned with the major axis, one aligned with the minor axis) and recovering the absolute phase of the sample, the image will once again be visually isotropic across the entire FOV while maintaining the advantage of compactness and large FOV gained from the mobile phone-based lens systems. Phase recovery also opens the doors to future exploration in aberration correction and super-resolution techniques such as Fourier Ptychography.

This chapter will be submitted as a paper entitled "Multi-Contrast Microscopy with Highly Non-Telecentric Compact Imaging Systems" by Daniel H. Friedman, Neil A. Switz, Kyoyeon Cho, and Daniel A. Fletcher.

Chapter 4

Dithering on a Mobile Phone-Based Platform

While contrast improvements widen the range of *types* of samples that are possible to image (e.g. light-absorbing vs transparent samples), resolution enhancement is required to widen the viewable range in *size* of samples. In order to improve field of view given a fixed sensor size, smartphone cameras typically undersample the optical image, placing limits on their use for low-cost microscopy and disease diagnosis. We implement dithering using the built-in optical image stabilizer to overcome sampling- and aliasing-related resolution limitations. This approach requires no additional hardware while providing an over 2x resolution enhancement for most smartphones based on a simple initial implementation.

4.1 Introduction

As a result of their extremely high manufacturing volumes, cellphone camera lenses are now extremely highly developed, featuring f-numbers as high as f/1.5 [86], as many as 6 elements of varying material composition, and $\geq$ 10 aspheric surfaces [47], allowing for excellent chromatic correction and nearly diffraction-limited performance across much of their field of view. Use of a similar lens as the objective of a microscope [45] enables imaging at a similar f/# across a field of view equivalent to the size of the camera sensor, 5.6 x 4.2mm, or $\approx$24mm^2, nearly an order of magnitude larger than the field of view of microscope objectives featuring similar numerical aperture. However, in order to increase field of view for a fixed pixel count, the modulation transfer function (MTF) at Nyquist for consumer and cellphone cameras is typically not zero, and can be tens of percent. Consequently aliasing occurs, especially on-axis where the point-spread function (PSF) is smallest (for this non-telecentric lens configuration, obliquity of the entrance pupil, in addition to the typical increased aberrations at larger field radii, will increase PSF off-axis, reducing aliasing there).

Aliasing is particularly unfortunate in cellphone microscopes because several important high-burden diseases are caused by parasites on precisely the size-scale the aliasing renders

inaccessible: particularly malaria parasites, which are of order $\approx 1\mu m$ and develop inside red blood cells ($\approx 8\mu m$ dia.). With an f/1.5 lens, we can calculate the potential resolution the system can achieve: since the f/# is ratio of the focal length f and the diameter of the lens d, the maximum light angle α equals $tan^{-1}(\frac{d/2}{f})$. The Rayleigh resolution is defined as $\frac{1.22\lambda}{2NA} = \frac{1.22\lambda}{2sin(\alpha)}$ (assuming fully incoherent illumination); thus, assuming a wavelength of 550nm (green light), we get a Rayleigh resolution of $1.06\mu m$.

Combined with the blue Giemsa stain for malaria parasites to increase contrast of infected red blood cells, such a lens system can in theory provide a resolution at the critical $1\mu m$ level. Reductions in aliasing-related resolution loss in such reversed-lens cellphone microscope systems would thus significantly improve the potential for diagnostics for this as well as other diseases.

Dithering has long been used to increase sampling frequency [87]. In many cases, the sampling offset can be chosen optically or mechanically such that additional samples are taken on a desired underlying grid. In such systems uniform sampling is assured via design, and any later image upsampling can be done via simple sinc-interpolation based on the Nyquist-Shannon sampling theorem. Other cases are more analogous to time-interleaved analog-to-digital conversion (e.g. in many oscilloscope analog-to-digital (ADC) systems) [88], where the sampling points are equally spaced, but sample trains from different ADCs have random relative offsets. This latter approach has the advantage of lower synchronization or control requirements (and thus lower cost), but the significant disadvantage that combining the separate sets of samples - in our case, multiple images with different displacements - onto a single uniform grid of points requires the mathematically significantly more complex interpolation of nonuniformly-spaced samples [89, 90].

Since our aim is for use in low-cost diagnostics, we make use of the built-in image stabilization system in modern cellphone cameras to enable image dithering with random offsets, followed by image-registration and reduction to a uniformly-sampled image. This requires no additional hardware, and enables potentially infinitely-dense sampling of the image, thus obviating aliasing issues and making the full resolution of the system accessible. We discuss theoretical considerations (maximum obtainable resolution, and related throughput), our dithering approach, and image reconstruction, in that order.

4.2 Methods

Obtainable Resolution

Imaging an object with a digital camera involves collecting and projecting light on a sensor, then digitally sampling that image. This amounts to the mathematical procedure:

$$O(x,y) \cdot PSF(x,y) \cdot Pixel(x,y) \circledast III(x,y)$$

where $O(x,y)$ is the object, the PSF is the incoherent optical PSF for the given f/# lens, and the sampling process is represented by a convolution of the image with the pixel active

area followed by sampling with a delta fence, $III(x, y)$. This set of delta functions may or may not represent sampling above Nyquist; however, in the limit of infinitely densely-spaced sampling, the best image that can be achieved – i.e. the limiting image quality – will thus be the convolution of the object with an effective PSF, $PSF_{effective} = PSF_{optical} \cdot Pixel$. We do not include any statistical averaging contribution related to the non-shift-invariance of the sampling process [91] because we subsequently dither to above Nyquist sampling and interpolate. The convolution relation indicates that the achievable resolution will be related to the sum of pixel width, d, and optical Rayleigh resolution, δ, and an effective Rayleigh resolution, defined by a 26.5% intensity dip between the point images.

From the preceding one can immediately define an effective optical transfer function (OTF), a hybrid of the incoherent optical MTF and the sinc from the averaging over the (square) pixel active area. Because the sinc has negative excursions (which correspond to contrast inversion at those spatial frequencies) we do not term this an effective MTF. This contrast inversion will begin at a spatial frequency of $\frac{1}{d}$, where d is the pixel width; the only way to avoid this is to use a system where the optical MTF is sufficiently small at the sinc zero that the effect is minor. This is not a trivial issue: some current cellphone lenses feature f/#s ≈ 1.5, corresponding to a maximum spatial frequency $2\frac{NA}{\lambda} = 1.45\mu m^{-1}$, yet utilize $1.4\mu m$ pixels [86] setting the first zero crossing at $0.765\mu m^{-1}$. Use of sensors with smaller pixels, or sufficient optical magnification M to reduce the sample-referenced pixel size, $\frac{d}{M}$, sufficiently are the only remedies (see figure 4.1).

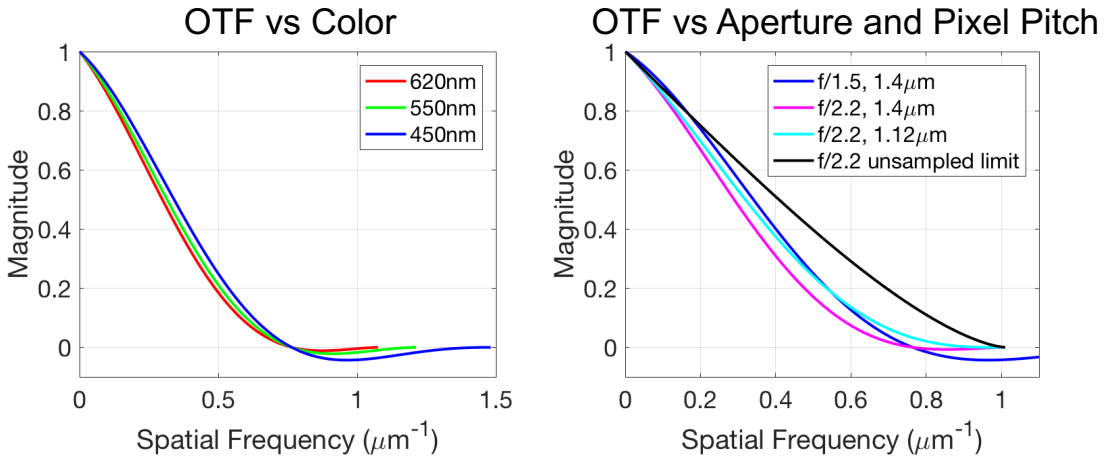

Figure 4.1: **Simulation of the (hybrid) optical transfer function for an optical system sampled by finite-width pixels.** Left: color dependance of a system with f/1.5 and $1.4\mu m$ pixel pitch. Right: Dependence on f/# and pixel pitch compared to the MTF of the diffraction-limited setup before sampling. Note that in this case where resolution is highly sampling limited, an improved f/# improves performance at lower spatial frequencies while reduction in pixel pitch improves high spatial frequency performance. Magnification on all plots is 1.07 to match the experimental setup.

Image sensors in cellphones are back-thinned, with a (typically) Bayer color filter array; thus pixel active area is square, with side $\leq d$, where d represents the pixel pitch. Red and blue pixels will be on an even grid of spacing $2d$; thus the function $Pixel(x, y) = rect(\frac{x}{d})$. Green pixels lie on a quincunxial array, effectively a grid of spacing $\sqrt{2}d$ rotated 45^o from the red/blue grids, from which aspect the function $Pixel(x, y) = triangle(\frac{x}{d})$. Performance varies with array orientation [92]; we are concerned here with the maximum obtainable. Typical values for a cellphone camera, e.g. the Samsung Galaxy S9, are $d = 1.4\mu m$, f/# = 1.5, and R, G, B center wavelengths for such color cameras are approximately 620nm, 550nm, and 450nm respectively. Using these definitions the effective OTF at Nyquist is 81% for red, 69% for green, and 77% for blue pixels; one can immediately see that imaging will be limited by aliasing (see figure 4.1). In the limit of infinitely-dense sampling, however, the limiting effective two-point resolution becomes $1.3\mu m$ in all three color channels (based on the first root of the sinc function associated with the pixel pitch). This represents a substantial improvement over the current best performance of $\approx 3\mu m$ monochrome resolution on-axis.

Experimental Setup: Dithering with the Built-In Optical Image Stabilizer

The optical image stabilizer embedded in most modern smartphones uses onboard angular accelerometers to predict the phone's movement relative to the object being imaged. Due to the purely feed-forward architecture of the system, these devices run under the assumption that the object's motion is fully independent of the phone's motion. However, that assumption breaks down when using the phone as a part of a mobile microscopy platform [39], where the sample is rigidly held in place relative to the phone. In this case, the image stabilizer still moves the lens to counteract the effect of the motion of the phone, but this lens translation now causes the field of view to translate relative to the fixed sample. This has the practical effect of offsetting the pixel sampling grid.

To gather the experimental datasets, a Galaxy S9 was fastened to a reversed lens setup focused on a USAF extreme resolution target in brightfield illumination. The phone was chosen due to its native ability to capture RAW images and because it leaves the image stabilizer on while the camera app is running (as opposed to only activating the stabilizer while exposing like iPhones do). This turns out to be a key functionality as the lens motion being used to gather offset images is also a source of motion blur if the lens moves by a large amount over the duration of the exposure. If the stabilizer is only activated during an exposure, it will also start the exposure at its center position, meaning that any motion necessary to cause a sufficient offset will also cause an appreciable blur. Conversely, if the stabilizer is constantly on, the phone can be moved to push the stabilizer into an offset position, and then the phone can be held still throughout the exposure.

To provide the required translational movement, the device was held by a steady human hand. The natural low-frequency vibration of the hand generated optical shifts on the order of 3 pixels in all directions. An Arduino system was set up to trigger the phone to capture

a RAW image every half second, plus or minus a random offset up to a tenth of a second to prevent steady motion patterns from appearing. Focus was locked at infinity, exposure was locked at 1ms, and ISO was locked at 50. Optical magnification was 1.07 due to the slight mismatch in focal lengths of the lenses (4.13mm for the S9 vs 4.03mm for the 6S) combined with the phone's inability to lock the focus exactly at infinity.

Algorithmic Approach

Although nonuniform images can be interpolated, this is complex [89, 90]. As this study is intended to show that the desired image resolution enhancement via dithering is possible, we implemented only the simplest version of this image acquisition, collecting sufficient images to select the required subset that fit naturally on a denser grid without interpolation. We leave for later work the implementation of the interpolation over nonuniform samples, with its expected reduction in total required images and thus imaging time.

After image collection, each photo was split into three images by creating a new matrix 4 times smaller than the original and populating it with only pixels of a given color. All images were then sub-pixel registered [93] to an accuracy of 1/10 pixel with respect to one another, and a final image containing m times the resolution was populated via a simple shift-and-add method for each color (in our particular experiment, $m = 5$: explanation in the following section). Due to the nature of sensor image stabilizers, as discussed above, we consider only translations of the sampling along the row and column axes (i.e., we exclude rotations). The result is 3 images, one for each color, each containing a non-interpolated resolution of 5 times the original image. Thus, the dithering in this case also allows for a demosaicing algorithm that did not require interpolation from pixels containing a different filter's color information (Figure 4.2).

Throughput

To calculate the expected number of photos required to fill all bins, it is first necessary to have a sense of the expected error (r) and m values to be used, where r is defined as twice the allowable distance between the registration point and the center of the sub-pixel bin (evaluated independently for the x and y axis). Thus, $r = 1$ means all images will be assigned to a bin, while $r \approx 0$ means only images with registrations that fall directly onto the center of a bin will be used.

For simplicity in analysis, we will use the values for our experimental setup. In the blue channel, the effective pixel spacing is $2.8\mu m$, yet Nyquist sampling of our potential limited resolution $1.3\mu m$ yields a required sampling spacing of $0.65\mu m$, 4.28 times smaller than the actual pixel spacing. Limiting the discussion to whole number binning, this means each pixel must be split into a minimum of 5 bins (per axis–25 bins total): $m = 5$.

However, the number of photos required depends both on the number of bins to fill and the probability that an image will not fit into any bin–i.e. the allowable error, r. Any positioning error of the registered image pixel positions from the precise centers of the expanded array

positions will introduce noise and error into the dithered image; the smaller these errors, the more closely the image will approach the best-case resolution discussed above.

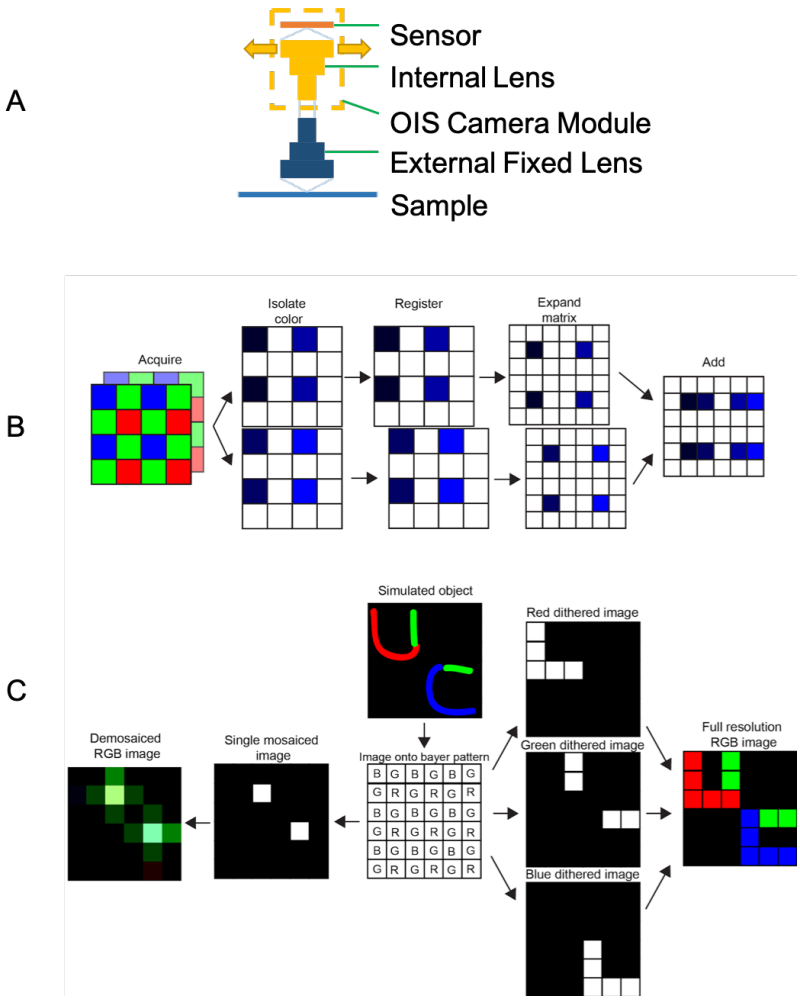

Figure 4.2: **Image processing workflow.** A) Dithering setup: A sample is fixed relative to the reversed lens setup. Then the optical image stabilizer shifts the internal phone lens, it also shifts the image of the sample. B) To dither each color channel, multiple images are acquired and color information is first isolated. Images subsequent to the first image are then registered, expanded, shifted, and added to generate an upsampled image. This process is repeated for each color channel. C) In addition to increasing sampling density, dithering eliminates the need for demosaicing to generate color images. A simulated object with multiple colors is shown. After capture with a Bayer-filtered sensor, the image can be demosaiced (interpolated) into a full resolution image, but much information is lost (left). Instead, if multiple images are taken and dithered to generate non-interpolated full-resolution images for each color, these images can simply be combined to generate a full-resolution RGB image.

A quantitative argument can be made that, in an ensemble average, the effect of assigning a new image pixel to a bin (of width $w = \frac{rd}{m}$) in which it falls is identical to convolving the image with an additional square of side w. The practical damage to the image will most likely be less, since the offsets of the 100+ images will be random, but assuming the worst case, a pixel of $2.8\mu m$, with the array expanded by $m = 5$, and using fractional acceptance $r = 1$, would result in convolution of the original object with another $2.8\mu m/5 = 0.5\mu m$ rect function. Given that the target resolution is $1.3\mu m$, this would be an over 40% further loss. Furthermore, image registration will not be perfect and thus will contribute to the rect and additional degradation of resolution.

A simple solution is to use an r value such that the above convolution kernel width is an order of magnitude smaller than the pixel width itself, with the assumption that effects on that scale will not be noticeable in practice. This imposes the constraint of $r = 0.1m$. However, this would require tossing a significant amount of photos that would not fit into a particular bin–adding more bins to relax the error constraint may actually reduce the number of photos required per acquisition.

Conveniently, image shifts generated by the setup are significantly larger than the pixel spacing, so the distribution of the centers of the shifted image pixels can be treated effectively flat, such that the probability of falling into a given array region is proportional only to the size of that region (see figure 4.3A). Thus, we can calculate the probability that all bins have at least one associated image as 1 - the probability that at least one bin is empty $P_{notfilled}$. The probability that one particular bin is empty $P(E_m)$ is

$$P(E_m) = \left(\frac{m^2 - r^2}{m^2}\right)^N$$

where N is the number of images taken ($N > m^2$). Invoking the inclusion-exclusion principle, we get:

$$P_{notfilled} = \binom{m^2}{1}\left(\frac{m^2 - r^2}{m^2}\right)^N - \binom{m^2}{2}\left(\frac{m^2 - 2r^2}{m^2}\right)^N + \binom{m^2}{3}\left(\frac{m^2 - 3r^2}{m^2}\right)^N - ...$$
$$+ (-1)^{m^2}\binom{m^2}{m^2 - 1}\left(\frac{m^2 - (m^2 - 1)r^2}{m^2}\right)^N (-1)^{m^2+1}\binom{m^2}{m^2}\left(\frac{m^2 - (m^2 r^2)}{m^2}\right)^N$$

Thus, the probability of all bins containing at least one image can be written as:

$$P_{filled} = 1 - P_{notfilled} = 1 - \sum_{k=1}^{m^2}(-1)^{k+1}\binom{m^2}{k}\left(\frac{m^2 - kr^2}{m^2}\right)^N$$

Figure 4.3B shows the probability curves for various combinations of m and r. The marginally dominating factor at $r > 0.5$ with the constant error width constraint is m; thus it is safe to assume for this particular case that minimizing m will also minimize the number of photos required. This assumption will break down for a setup that requires a small r.

Figure 4.3C provides the expected number of photos required to have a 90% chance of all bins being filled, given different sample constraints. For the usual full-color approach, an m of 5 and r of 0.5 was optimal.

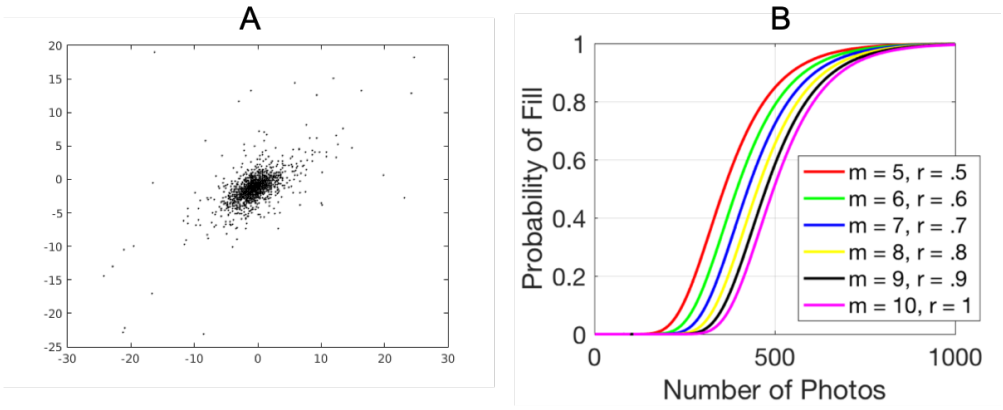

C

	m	r	# of photos
Full Color	5	0.5	545
Monochrome Green	3	0.5	159
Monochrome Colorless	3	0.6	110

Figure 4.3: **Measuring probable throughput.** A) Distribution of image registration offsets taken with the OIS-dithering setup. B) Probability of all bins having at least one assigned image for various combinations of binning and allowed error. C) Expected number of photos required to fill all bins with 90% probability. If an image is taken purely for monochrome measurement through the green filter, the equivalent pixel size is 71% that of the blue or red pixels due to the quincunxial pattern. Error remains the same as the full color image to keep the absolute kernel width constant. If the sample being imaged is entirely colorless, a previously taken image of a pure white sample can be used to calibrate out the difference in color sensitivities between the three colors, allowing for a monochrome image with sampling density equal to the pixel pitch of the sensor. Values in (C) were verified via Monte Carlo simulation and experimental data.

4.3 Results

In order to quantitatively test our dithering workflow, we took multiple images of a USAF extreme resolution target. An example of the resolution obtained per color channel by our system is shown in Figure 4.4A. Here, the elements of group 8 of the target are clearly

unresolvable. The images were registered and processed by the method explained above, and the dithered blue color channel is shown in Figure 4.4B, where the beginning elements of group 9 are clearly visible. To examine the contribution of noise to our obtainable resolution, we repeat this same process, but instead of limiting each bin to only one image, any bin with multiple assigned images will keep an averaged value of all those images. While using multiple images per bin does not improve resolution, it does noticeably reduce noise in the image.

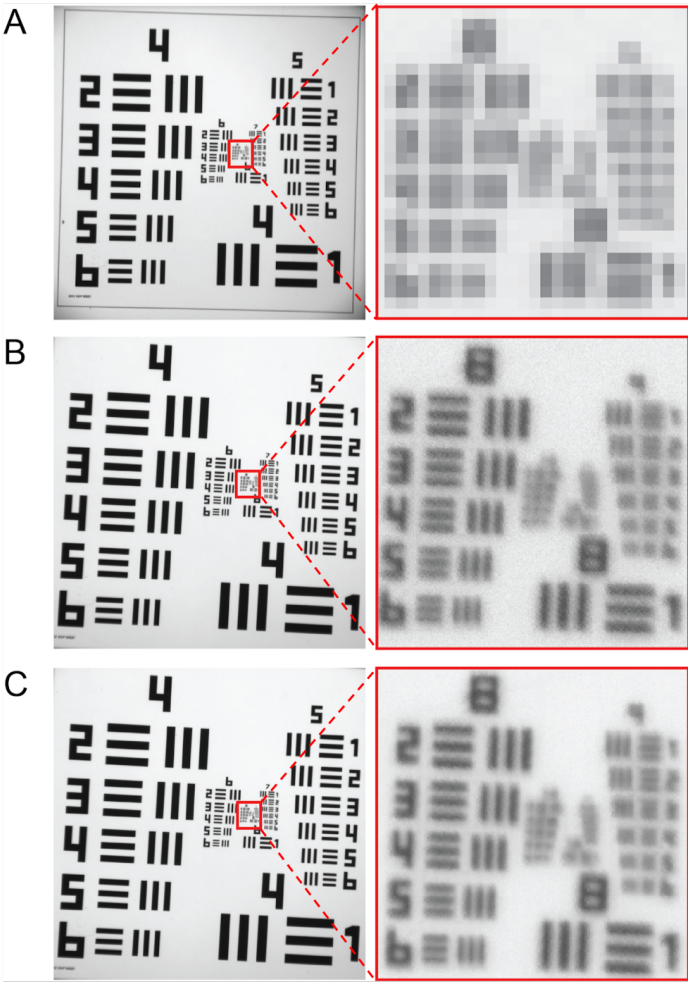

Figure 4.4: **Dithering combined with shift-and-add image synthesis enables enhanced resolution imaging.** A) An image of a portion of a USAF with only the blue pixels of the raw image. For display, image is nearest neighbor interpolated. B) 100 shifted-and-added blue-pixel images (one for each position in the expanded matrix) of the same portion of a USAF target. 100% coverage was reached after 654 images were processed ($m = 10$, $r = 1$). For display, image is nearest neighbor interpolated. C) The same as B), except with multiple images averaged into each bin (1613 images total).

Dithering produces full resolution, non-interpolated images for each color channel

Next, we sought to test whether full resolution color images could be reconstructed using our same USAF extreme resolution target. An example of a standard demosaiced color is shown in Figure 4.5A. The process of demosaicing interpolates missing colors for each position of the Bayer pattern. Therefore, if an object has features on the same size-scale as the Bayer pattern, the spatial features will be interpreted instead as color information. This results in the repeating color pattern seen along what should be sharp, black edges in Figure 4.5A. By dithering each color channel and then combining them to generate an RGB image, full resolution can be obtained for each color channel without interpolation and the mixing of spatial and color information (Figure 4.5B).

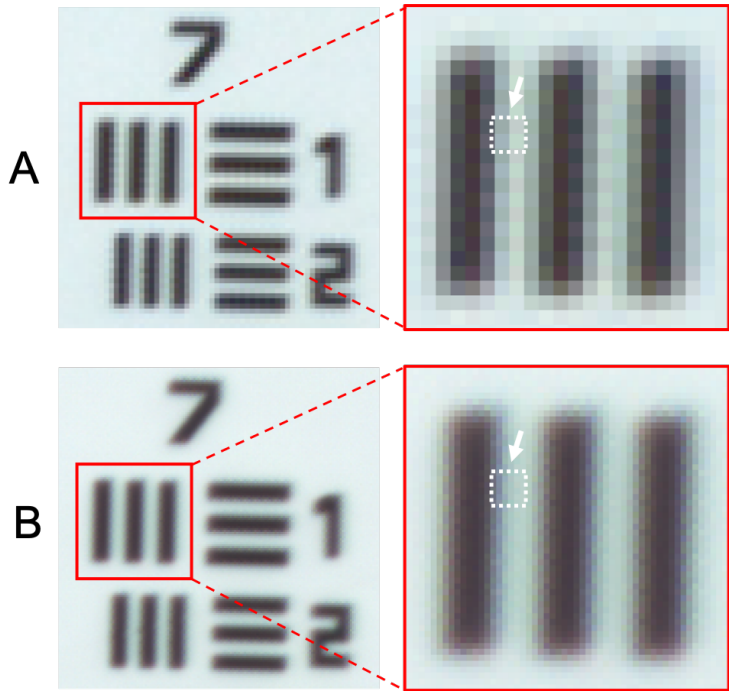

Figure 4.5: **Dithering combined with shift-and-add image synthesis enables full resolution color image acquisition.** A) A demosaiced color image of a portion of a USAF target. White box and arrow (right pane) indicate the unit of a repeating pattern of spatial information falsely encoded as color by the demosaicing process. B) A dithered color image of the same portion of a USAF target, computed by repeating the process in Figure 3C for each color ($m = 5$, $r = 0.5$ – 1613 images total).

Dithering produces higher-resolution of images of real samples

To demonstrate the resolution gain that can be obtained by dithering real samples, we imaged stained trypanosomes and malaria on a thin human blood smear (figure 4.6).

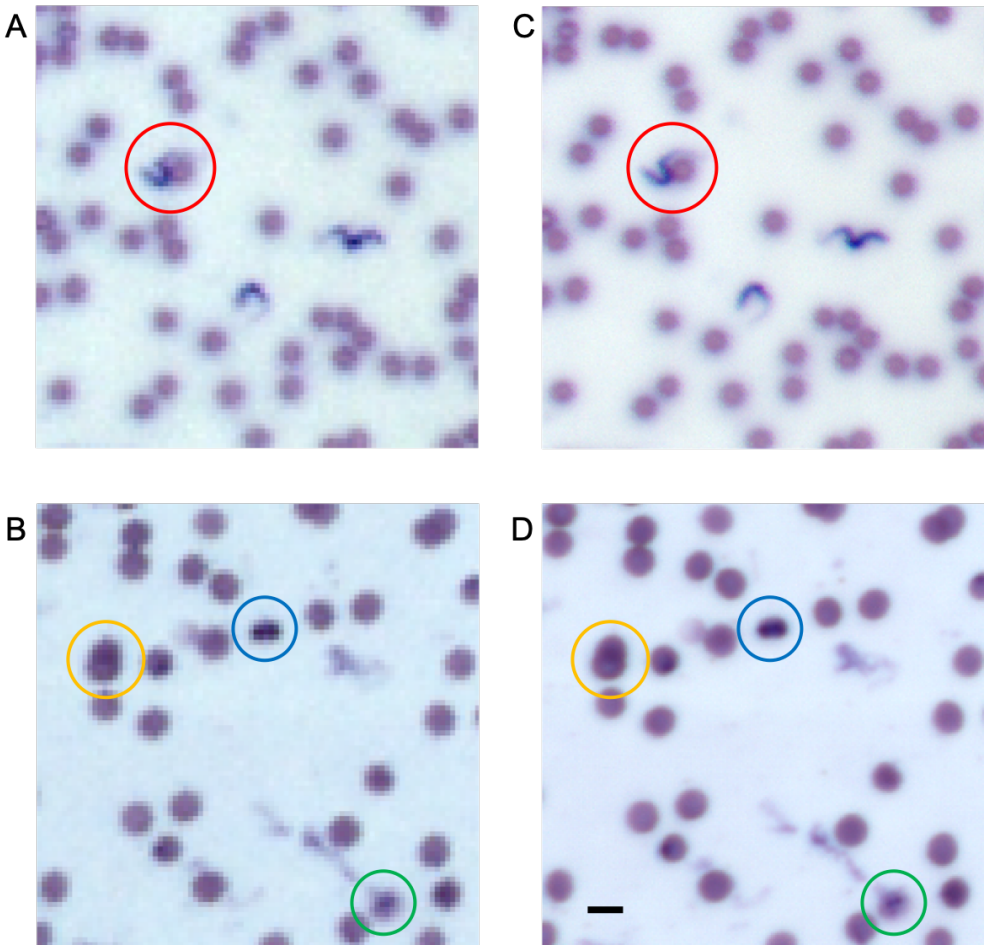

Figure 4.6: **Comparison of single-frame and dithered images.** A) A raw image of stained trypanosomes. B) A dithered image of the same region as A ($m = 5$, $r = 0.5$, 2571 images). Note the substantial improvement in detail for low-contrast overlapping features like the trypanosome tail next to a red blood cell (red circles). C) A raw image of a Giemsa-stained malaria thin smear. D) A dithered image of the region as C ($m = 5$, $r = 0.5$, 1613 images). Again, note the improvement in detail for overlapping features (orange circles). Also note the emergence of detail between stained areas and surrounding cell structure (blue circles), along with emergence of shape for punctate structures (green circles). Since it was not possible to turn off the OIS, raw images were generated by registering whole-pixel-shifted images together and averaging to obtain the same SNR as the dithered images. Scale bar: $10\mu m$.

4.4 Discussion

Here we have reported a theoretical limit and practical implementation of OIS dithering for the reversed lens optical system. While theory predicts up to group 9,4 of the USAF target being resolvable, experimentally we only find that group 9,2 is clearly discernible. However, as predicted contrast is $< 10\%$ for resolutions above group 9,2, we find that experimental results are consistent with theory. This lends credit to the conclusion that the pixel width is the dominant factor in limiting resolution, where the general rule applies that dithering-limited resolution will be improved by a factor of approximately 2x from the sampling-limited resolution (not including Bayer filter effects) until the actual diffraction limit of the optics applies.

While other commercial systems (Google Pixel Phone, Panasonic mirrorless cameras) have been reported to use dithering to boost sampling density, the exact manipulations that they perform are unknown. Similarly to proprietary demosaicing used by many cameras, one must be cautious of use of data capture devices that use non open-source algorithms to process images. A key goal of this work was to demonstrate that the resolution of a mobile microscope based on the reversed lens system could be improved to extend the range of pathogens that it could detect with a simple algorithm that is compatible with medical imaging. Here we show that imaging of trypanosome and malaria parasites is clearly improved: trypanosome morphology is significantly clearer, especially in areas of overlap with other structures (e.g. red blood cells); and basic components of intracellular morphology are apparent in the dithered malaria images where only colorimetric data was visible in the raw image.

It is worth reiterating here that this study was meant to introduce the idea of OIS-based dithering, and has therefore left out advanced optimization from the experimental methods. Several improvements can be made with added assumptions. First, the number of images required can be reduced by approximately an order of magnitude if the OIS is manually controlled instead of randomly moved. This would also ameliorate the issue of motion blur as the stabilizer can be held in place throughout the exposure, thus opening the door to low-light/fluorescence dithering. Controlling the OIS is unlikely to be possible in unmodified smartphones, but may be feasible in more customized setups.

There is also room for improved resolution performance. We assumed anything past the contrast inversion point in the OTF was at too low of contrast to be useful. However, with a high enough SNR, the image can theoretically be deconvolved to recover contrast on either side of the inversion point (note that only the sinc multiplication can be easily deconvolved, as the other optical attributes of the system are not shift-invariant). Even without deconvolution, the low-contrast information may still be useful for computer vision algorithms. There is also room for existing dithering algorithms, such as the "drizzle" algorithm used by the Hubble Space Telescope, to improve performance by making assumptions about the sample (e.g. sparse, punctate sources).

Lastly, there are a few key unknowns in the demonstrated system that should be mentioned. The optical effects of moving only the camera lens (and thus slightly misaligning the

optical track) will vary extensively depending on chosen lens combinations, but will likely contribute to some level of increased aberration, especially at the edges of the field of view. Given that the edge of the field of view is already aberration limited, and not sampling limited [45], dithering via this method may actually impair the resolution in these regions. Finally, accurate sub-pixel registration, especially of samples with color information where pixel-wide gaps between samples will be present, is only possible when an ensemble of features are spread over multiple pixels with fractional pixel spacing. For the purposes of this study, we have assumed that our samples were sufficiently information-rich to satisfy this criteria and that registration performed well enough to not significantly impact the results.

This chapter will be submitted as a paper entitled "Improving Resolution of Mobile Phone Microscopes via Optical Image Stabilizer Dithering" by Daniel H. Friedman, Michael V. D'Ambrosio, Neil A. Switz, and Daniel A. Fletcher.

Chapter 5

Concluding Remarks

5.1 Dissertation Summary

Overall, the goal of this dissertation was to highlight the necessity for a portable diagnostic platform, and to describe and solve a few of the key challenges that come up in the process of designing such a device. In Chapter 1, I detailed the discrepancies between health care in developed countries versus developing countries, and provided an overview of the main causes of those discrepancies. I then gave a series of examples of potential solutions to bridge access to modern diagnostic care, including the work done by this lab before I joined. Finally, I went over the basics of digital cameras and phone lenses specifically in the context of how mass production has created a low-cost yet high-tech resource that can be adapted for medical use.

In Chapter 2, I explained the basic concepts behind the three contrast modalities built into the PlantScope and detailed the assumptions made behind the practical implementation of those modalities. I also briefly mentioned potential improvements to those implementations for the next generation of devices, especially for fluorescence. I then provided an example use case where we set up a field study in the Philippines to detect Fusarium in soil samples. This section detailed why Fusarium detection is important, the protocol developed for testing on-site, and preliminary results of the trial.

In Chapter 3, I took a deep dive into the main challenge in achieving uniform contrast with a mobile phone-based microscope: non-telecentricity. Then, after a quick aside on the theory of DPC itself, I proposed a method for recovering uniform contrast by taking a multitude of strategically illuminated images. Finally, I explored the potential artifacts introduced into the final image as a side effect of the proposed method.

Finally, in Chapter 4, I proposed a method of improving the resolution of the reversed lens system. I detailed the sources of loss in resolution performance, introduced dithering as a method of recovering some of that performance, and also introduced a method of dithering that did not involve extra hardware or any modification of the phone. I then showed results on resolution targets and parasite samples as proof of the enhanced performance the dithering

protocol could provide.

5.2 Advice for Future Global Health Technology Developers

The Future of Screen-Based Illumination

While Chapter 3 focused mainly on the DPC algorithm, I purposely glossed over the use of an LCD screen as the illumination source. The reason is that I don't believe there is a future for screen-based illumination in mobile microscopy. Even with a nice camera and the iPad screen on full brightness, it took at least a second's worth of exposure (either by directly exposing, or by averaging) to get an image with an acceptable SNR. The iPad screen is also enormous, making it great for experimental setups, but terrible as a mobile platform.

So for screen illumination to be practical, the screens need to be smaller and brighter. There are three factors standing in the way. First, making the screen smaller is more complicated than expected. The smaller it is, the closer it needs to be to the lens to fully illuminate the field of view. The closer it is, the more densely packed the pixels need to be to maintain the necessary angular control (less than 1 degree for the patch DPC approach). Also, the DPC algorithm assumes the light from any particular pixel shines over the entire sample from exactly one angle (within about a half degree). At 40mm or more away, that assumption holds true; but at 10mm away, a 5mm-wide field of view will see drastically different angles from the same pixel. This makes the illumination scheme significantly more challenging (though potentially not impossible).

The last main issue with using a smaller screen is that no phone manufacturer makes that tiny of a screen (4cm x 4cm would probably be ideal). That means we need to rely on OEM or hobbyist boards, which lag behind the latest tech by years. For example, the few LCD modules we tried from Adafruit were about four times dimmer than the iPad, with about one third the pixel density.

The logical conclusion here is that eventually the technology will catch up. Screens have been getting brighter and higher density, so the hobbyist boards will eventually do the same. Unfortunately, this falls short as well. The LED-based lights we've been using to get reasonable exposures hurt your eyes to look at, even in full daylight. Phone screen manufacturers will never make a screen that bright because no one would need it (especially when it is at the expensive of battery life). And the final nail in the coffin is that LCD technology is giving way to AMOLED screens, which have all but dominated the high-end small screen market as of this writing. While AMOLED screens have many advantages for the typical user, their use of PWM to control brightness of individual pixels makes it impossible to expose an image below 300ms.

All in all, the conclusion I've come to is that screens are extremely useful for experimental setups where exposure time and size aren't an issue. But technology just isn't evolving in the right direction for them to be useful in the field.

The Future of Non-Telecentric DPC

So where does that leave reversed-lens DPC? Chapter 2 showed repeatedly that small assumptions can lead to drastically simplified systems that accomplish the same contrast with acceptable artifacts. I believe the same can be done with DPC. At its heart, DPC just needs light from angles from one side of the origin to be subtracted from light on the other side of the origin. Doing so retains the phase information while dumping the amplitude information.

The solution I came up with is to use the sample translation to change the angles, and illuminate only the center of the field of view with a narrow line of illumination perpendicular to the direction of motion. The line can be made with a row of LED's run through a narrow diffuser. The range of angles emitted along the narrow direction must be less than the maximum collection angle defined by the objective NA (explanation below). In essence, this creates one giant vertical patch. For setups that only have one degree of motorized freedom (like the LoaScope), this means DPC can only be done in one axis; but it's still a way to get phase.

Here is the process: For discussion purposes, let's say our setup has a maximum acceptance angle of X degrees and a maximum field angle of Y degrees along the horizontal axis. We will have a vertical line of illumination at the horizontal center of the FOV. The left edge of that illumination line will reach the area of the FOV corresponding to $-X/4$, and the right edge of the line will reach to $+X/4$. We start our scan with the right edge of the light just barely hitting the left edge of the sample. Then, moving the sample left in very small increments (less than a the equivalent of a degree shift in field angle in the middle of the FOV), we take an image at each increment until the light is no longer hitting the sample. Also at some point, we need to take a blank image for normalization.

Now we have a dataset where, for each image, we know exactly what angles of light (in the horizontal axis) are illuminating each pixel in the FOV. By registering all the photos, we get a final dataset where each point on the sample has a series of photos where it has been illuminated from every possible brightfield angle (along with many darkfield angles). Now for each sample point, we find the photos where it was only illuminated between $-X$ and 0 degrees, divide each photo by the blank photo (to normalize for the varying intensity across the FOV), and add them together. This gives us one of our half DPC images, and doing the same for 0 to $+X$ degrees gives us the other half. Finally, we subtract and divide like a normal DPC process to get our final DPC image (or just add the two to get brightfield). Adding up everything outside the brightfield regions of each image (before normalization) gives a darkfield image.

This process involved a few key assumptions. First, the sample can't move (e.g. wriggling worms, etc). Second, while analysis from chapter 3 shows that darkfield contributions from the left or the right of the line would cause significant shading effects (hence making the line narrow enough to ensure there will be useable images), I'm assuming that the darkfield contributions perpendicular to the line of travel will be the same in both half images, and thus be cancelled out. The last assumption is that a mobile processor will be able to do all this image stitching and processing in a reasonable amount of time. At some point, that will

likely be true.

Incorporating Dithering into a Field-Ready Device

After working with this technology for a while, I'm convinced that dithering with play an important role in any mobile device that uses the reversed lens system. Chapter 4 showed the potential resolution gains from shrinking the effective size of the pixels, which is essential for high-resolution imaging with sensors that have been specifically designed to drastically undersample. Equally as important is the ability to accurately separate color from intensity information since the two are innately coupled from the bayer filter setup. Optical image stabilization will only become more common over time as market pressures force manufacturers to make better and better phone cameras, especially for smooth video and low-light performance; this insures that this method of dithering will be possible for the foreseeable future.

I also want to mention a potential new direction phone cameras are taking that was not mentioned in chapter 4. As of late 2018, Sony and Samsung both released a new style of sensor with a larger area and smaller pixel pitch (Sony IMX586 and Samsung ISOCELL Bright GM1), resulting in a 48MP camera that natively bins to 12MP [94, 95]. Given the size of the sensor, it will be possible to magnify the image by around 1.3X and still maintain a 5mm field of view. That gives an effective pixel pitch of 600nm, which is just about at Nyquist frequency. Rather than seeing this new development as an alternative to dithering, I think it opens the doors for alternate ways to dither.

While it is true that resolution gains will be limited, the color/intensity separation will still be an issue, especially since the Bayer filters used have four pixels under each color instead of one (effectively creating a $1.6\mu m$ pixel pitch). Since we would only need to move the pixels around to gain color information instead of actual spatial frequency recovery, it should be possible to use any motile device (such as the motorized stage) to get enough movement. That simplifies the sensor module (no OIS required), which will reduce cost and improve reliability. The main question now is whether these new high-density sensors will really become the new standard for high-end cameras.

5.3 Concluding Thoughts on the Ph.D.

As always is the way with science, exploring the answers to the issues described in this dissertation only brought up more questions. To me, that's the best part: when you've finally delved so deeply into a field that you think of questions no one has asked before, yet who's answers could solve a problem everyone has been thinking about. And that leads to the most important lesson I learned as a Ph.D. student–you need to put in the effort to get the knowledge to ask the right questions. But once there, curiosity quickly becomes an infinite source of inspiration. The DPC project began when, just for the heck of it, I tried to run the standard DPC illumination on the reversed lens system just to see what would

happen. The algorithm seemed to work in the center of the field of view, so why couldn't I make it work elsewhere? The entire dithering chapter was based off of a random thought I had while tinkering with my phone: I wonder if the optical image stabilizer controller has any feedback. I needed the background knowledge of how these things worked to ask those questions. I also needed that background knowledge to begin the search for the answers. And that same strategy sets Ph.D's apart from the rest. We traded five or six years of in-field experience with five or six years of learning how to bring the problem back to basic principles and build a solution far more robust than experience alone could create. So my last piece of advice to any Ph.D. student reading this is to keep that in mind the value of this degree and tailor your work to maximize that skill. The effort really does pay off.

Bibliography

[1] World Health Organization. "GLOBAL ACTION PLAN FOR THE PREVENTION AND CONTROL OF NONCOMMUNICABLE DISEASES iii WHO LIBRARY CATALOGUING-IN-PUBLICATION DATA". In: *World Health Organization* (2013), p. 102. ISSN: 0003-990X. DOI: ISBN9789241506236. arXiv: arXiv:1011.1669v3. URL: www.who.int/about/licensing/copyright%7B%5C_%7Dform/en/index.html%7B%%7D5Cnhttp://apps.who.int/iris/bitstream/10665/94384/1/9789241506236%7B%5C_%7Deng.pdf?ua=1%7B%%7D0Awww.who.int/about/licensing/copyright%7B%5C_%7Dform/en/index.html.

[2] Aranka Anema et al. "Digital surveillance for enhanced detection and response to outbreaks". In: *The Lancet Infectious Diseases* 14.11 (2014), pp. 1035–1037. ISSN: 14744457. DOI: 10.1016/S1473-3099(14)70953-3. URL: http://dx.doi.org/10.1016/S1473-3099(14)70953-3.

[3] CDC. "CDC and Malaria in the United States". In: (2017). URL: https://www.cdc.gov/malaria/resources/pdf/fsp/cdc%7B%5C_%7Dmalaria%7B%5C_%7Ddomestic%7B%5C_%7Dunit.pdf.

[4] *Guide to Pre-Travel Consultation*. 2018. URL: https://www.cdc.gov/thinktravel/pdf/Think-Travel-Pre-Travel-Guide-508.pdf (visited on 03/03/2019).

[5] Gary W Brunette. *CDC Yellow Book 2018*. Ed. by Gary W Brunette. 2017, p. 704. ISBN: 9780190628611.

[6] Damian G. Walker et al. "Poverty and Access to Health Care in Developing Countries". In: *Annals of the New York Academy of Sciences* 1136.1 (2008), pp. 161–171. DOI: 10.1196/annals.1425.011.

[7] *World health statistics 2018: monitoring health for the SDGs, sustainable development goals*. Geneva: World Health Organization, 2018. ISBN: 9789241565585. URL: http://e-journal.uajy.ac.id/14649/1/JURNAL.pdf.

[8] Pablo Gottret and George Scheiber. *Health Financing Revisited*. Washington DC: The International Bank for Reconstruction and Development / The World Bank, 2006, p. 340. ISBN: 9780821365854.

[9] Nazmul Chaudhury and Jeffrey S. Hammer. "Ghost doctors: Absenteeism in rural Bangladeshi health facilities". In: *World Bank Economic Review* 18.3 (2004), pp. 423–441. ISSN: 02586770. DOI: 10.1093/wber/lhh047.

[10] Kara Hanson et al. "Expanding access to priority health interventions: A framework for understanding the constraints to scaling-up". In: *Journal of International Development* 15.1 (2003), pp. 1–14. ISSN: 09541748. DOI: 10.1002/jid.963.

[11] Shanthi Mendis et al. "The availability and affordability of selected essential medicines for chronic diseases in six low- and middle-income countries". In: *Bulletin of the World Health Organization* 85.May 2007 (2007), pp. 279–288. ISSN: 0042-9686. DOI: 10.1590/S0042. URL: http://www.who.int/bulletin/volumes/94/9/16-181636/en/http://dx.doi.org/10.2471/BLT.16.181636.

[12] John S. Akin and Paul Hutchinson. "Health-care facility choice and the phenomenon of bypassing". In: *Health Policy and Planning* 14.2 (1999), pp. 135–151. ISSN: 02681080. DOI: 10.1093/heapol/14.2.135.

[13] Sjaak Van Der Geest. "Self-care and the informal sale of drugs in South Cameroon". In: *Social Science and Medicine* 25.3 (1987), pp. 293–305. ISSN: 02779536. DOI: 10.1016/0277-9536(87)90232-2.

[14] Stephen E Weis et al. "The Effect of Directly Observed Therapy on the Rates of Drug Resistance and Relapse in Tuberculosis". In: *New England Journal of Medicine* 330.17 (1994), pp. 1179–1184. ISSN: 0028-4793. DOI: S0008-6363(04)00366-9[pii]10.1016/j.cardiores.2004.08.007.

[15] N. J. White. "Preventing antimalarial drug resistance through combinations". In: *Drug Resistance Updates* 1.1 (1998), pp. 3–9. ISSN: 13687646. DOI: 10.1016/S1368-7646(98)80208-2.

[16] Simon L Croft, Shyam Sundar, and Alan H Fairlamb. "Drug Resistance in Leishmaniasis". In: *Clinical Microbiology Reviews* 19.1 (2006), pp. 111–126. ISSN: 00185973. DOI: 10.1128/CMR.19.1.111.

[17] S.A. Boppart and R. Richards-Kortum. "Point-of-care and point-of-procedure optical imaging technologies for primary care and global health". In: *Science Translational Medicine* 6.253 (2014). ISSN: 1946-6242. DOI: 10.1126/scitranslmed.3009725. URL: http://www.embase.com/search/results?subaction=viewrecord%7B%5C&%7Dfrom=export%7B%5C&%7Did=L600075929%7B%%7D0Ahttp://dx.doi.org/10.1126/scitranslmed.3009725%7B%%7D0Ahttp://lh.cineca.it/Ccube/openclink.do?sid=EMBASE%7B%5C&%7Dsid=EMBASE%7B%5C&%7Dissn=19466242%7B%5C&%7Did=doi:10.1126%7B%%7D2Fscitranslmed.3009725%7B%5C&%7Datitle=.

[18] H. W. Choi et al. "Cost-effectiveness of Xpert®MTB/RIF for diagnosing pulmonary tuberculosis in the United States". In: *International Journal of Tuberculosis and Lung Disease* 17.10 (2013), pp. 1328–1335. ISSN: 10273719. DOI: 10.5588/ijtld.13.0095.

[19] Samuel Shillcutt et al. "Cost-effectiveness of malaria diagnostic methods in sub-Saharan Africa in an era of combination therapy". In: *Bulletin of the World Health Organization* 86.2 (2008), pp. 81–160.

[20] Mahendra Pratap Singh and Manoj Kumar Jain. "Evolution of Processor Architecture in Mobile Phones". In: *International Journal of Computer Applications* 90.4 (2014), pp. 34–39.

[21] Adam Sinicki. *Are smartphones still getting faster? Does Moore's law still apply?* 2017. URL: https://www.androidauthority.com/smartphone-speed-moores-law-801776/ (visited on 02/20/2019).

[22] Hatice Ceylan Koydemir and Aydogan Ozcan. "Smartphones Democratize Advanced Biomedical Instruments and Foster Innovation". In: *Clinical Pharmacology and Therapeutics* 104.1 (2018), pp. 38–41. ISSN: 15326535. DOI: 10.1002/cpt.1081.

[23] Hongying Zhu et al. "Optical imaging techniques for point-of-care diagnostics". In: *Lab on a Chip* 13.1 (2013), pp. 51–67. ISSN: 14730189. DOI: 10.1039/c2lc40864c. arXiv: NIHMS150003.

[24] Onur Mudanyali et al. "Compact, light-weight and cost-effective microscope based on lensless incoherent holography for telemedicine applications". In: *Lab on a Chip* 10.11 (2010), pp. 1417–1428. ISSN: 14730189. DOI: 10.1039/c000453g. arXiv: NIHMS150003.

[25] Chulwoo Oh et al. "On-chip differential interference contrast microscopy using lensless digital holography". In: *Optics Express* 18.5 (2010), p. 4717. ISSN: 1094-4087. DOI: 10.1364/OE.18.004717. arXiv: NIHMS150003. URL: https://www.osapublishing.org/oe/abstract.cfm?uri=oe-18-5-4717.

[26] Derek Tseng et al. "Lensfree microscopy on a cellphone". In: *Lab on a Chip* 10.14 (2010), pp. 1787–1792. ISSN: 14730189. DOI: 10.1039/c003477k. arXiv: NIHMS150003.

[27] Alon Greenbaum et al. "Imaging without lenses: Achievements and remaining challenges of wide-field on-chip microscopy". In: *Nature Methods* 9.9 (2012), pp. 889–895. ISSN: 15487091. DOI: 10.1038/nmeth.2114. arXiv: NIHMS150003.

[28] Waheb Bishara et al. "Holographic pixel super-resolution in portable lensless on-chip microscopy using a fiber-optic array". In: *Lab on a Chip* 11.7 (2011), pp. 1276–1279. ISSN: 14730189. DOI: 10.1039/c0lc00684j. arXiv: NIHMS150003.

[29] S. Seo et al. "High-throughput blood analysis on a chip using lensless digital holography". In: *14th International Conference on Miniaturized Systems for Chemistry and Life Sciences 2010, MicroTAS 2010* 2.11 (2010), pp. 1424–1426. DOI: 10.1364/OL.30.000468.

[30] Onur Mudanyali et al. "Detection of waterborne parasites using field-portable and cost-effective lensfree microscopy". In: *Lab on a Chip* 10 (2010), pp. 2419–2423. DOI: 10.1039/c004829a.

[31] James S. Cybulski, James Clements, and Manu Prakash. "Foldscope: Origami-based paper microscope". In: *PLoS ONE* 9.6 (2014). ISSN: 19326203. DOI: 10.1371/journal.pone.0098781. arXiv: 1403.1211.

[32] James S. Cybulski et al. *foldscope.com*. 2018. (Visited on 01/05/2018).

[33] Zachary J Smith et al. "Cell-Phone-Based Platform for Biomedical Device Development and Education Applications". In: 6.3 (2011). DOI: 10.1371/journal.pone.0017150.

[34] Zachary J Smith, Kaiqin Chu, and Sebastian Wachsmann-hogiu. "Nanometer-Scale Sizing Accuracy of Particle Suspensions on an Unmodified Cell Phone Using Elastic Light Scattering". In: *PLoS ONE* 7.10 (2012), pp. 1–7. DOI: 10.1371/journal.pone.0046030.

[35] Sara Kheireddine et al. "Lab on a Chip microscopy". In: *Lab on a Chip* 19.1 (2019), pp. 825–836. DOI: 10.1039/c8lc00995c.

[36] Division Molecular Biotechnology et al. "Mobile microscopy for the examination of blood samples". In: *EMBnet.journal* 23 (2018), e904. DOI: 10.14806/ej.23.0.904.

[37] *Oculyze.de*. 2018. URL: https://www.oculyze.de/en-us/.

[38] David N. Breslauer et al. "Mobile phone based clinical microscopy for global health applications". In: *PLoS ONE* 4.7 (2009), pp. 1–7. ISSN: 19326203. DOI: 10.1371/journal.pone.0006320.

[39] M.V. D'Ambrosio et al. "Point-of-care quantification of blood-borne filarial parasites with a mobile phone microscope". In: *Science Translational Medicine* 7.286 (2015), no pagination. ISSN: 1946-6242. DOI: 10.1126/scitranslmed.aaa3480. URL: http://stm.sciencemag.org/content/7/286/286re4.full.pdf%7B%%7D5Cnhttp://ovidsp.ovid.com/ovidweb.cgi?T=JS%7B%5C&%7DPAGE=reference%7B%5C&%7DD=emed17%7B%5C&%7DNEWS=N%7B%5C&%7DAN=604293698.

[40] Asa Tapley et al. "Mobile digital fluorescence microscopy for diagnosis of tuberculosis". In: *Journal of Clinical Microbiology* 51.6 (2013), pp. 1774–1778. ISSN: 00951137. DOI: 10.1128/JCM.03432-12.

[41] Jean T. Coulibaly et al. "Accuracy of Mobile Phone and Handheld Light Microscopy for the Diagnosis of Schistosomiasis and Intestinal Protozoa Infections in Côte d'Ivoire". In: *PLoS Neglected Tropical Diseases* 10.6 (2016), pp. 1–10. ISSN: 19352735. DOI: 10.1371/journal.pntd.0004768.

[42] Robi N. Maamari et al. "A mobile phone-based retinal camera for portable wide field imaging". In: *British Journal of Ophthalmology* 98.4 (2014), pp. 438–441. ISSN: 14682079. DOI: 10.1136/bjophthalmol-2013-303797.

[43] L. H. Chaisson et al. "Evaluation of mobile digital light-emitting diode fluorescence microscopy in Hanoi, Viet Nam". In: *International Journal of Tuberculosis and Lung Disease* 19.9 (2015), pp. 1068–1072. ISSN: 10273719. DOI: 10.5588/ijtld.15.0018.

[44] Robi N. Maamari et al. "Novel Telemedicine Device for Diagnosis of Corneal Abrasions and Ulcers in Resource-Poor Settings". In: *JAMA Ophthalmology* 132.7 (2014), p. 894. ISSN: 21686165. DOI: 10.1001/jamaophthalmol.2014.335. URL: http://archopht.jamanetwork.com/article.aspx?doi=10.1001/jamaophthalmol.2014.335.

[45] Neil A. Switz, Michael V. D'Ambrosio, and Daniel A. Fletcher. "Low-cost mobile phone microscopy with a reversed mobile phone camera lens". In: *PLoS ONE* 9.5 (2014). ISSN: 19326203. DOI: 10.1371/journal.pone.0095330.

[46] Joseph Kamgno et al. "A Test-and-Not-Treat Strategy for Onchocerciasis in Loa loa - Endemic Areas". In: *New England Journal of Medicine* (2017), NEJMoa1705026. ISSN: 0028-4793. DOI: 10.1056/NEJMoa1705026.

[47] P-L Hsu and H-H Huang. *Image capturing optical lens system*. 2014.

[48] Nayeem Islam and Roy Want. "Smartphones: Past, present, and future". In: *IEEE Pervasive Computing* 13.4 (2014), pp. 89–92. ISSN: 15361268. DOI: 10.1109/MPRV.2014.74.

[49] Dave Litwiller. "CCD vs CMOS: Facts and Fiction". In: *Photonics Spectra* January (2001), pp. 1–4. ISSN: 0731-1230. URL: papers3://publication/uuid/56A8BFC6-C44A-4056-AA0D-37A8AAE33BA6.

[50] M. Bigas et al. "Review of CMOS image sensors". In: *Microelectronics Journal* 37.5 (2006), pp. 433–451. ISSN: 00262692. DOI: 10.1016/j.mejo.2005.07.002.

[51] Ray Fontaine. "The State-of-the-Art of Mainstream CMOS Image Sensors". In: *Proc. 2015 International Image Sensor Workshop* (2015).

[52] Dan Croucher. "Increasing CMOS Camera Sensitivity Through Back- Illumination". In: *Photometrics* (2017), pp. 1–9.

[53] Bryce E Bayer. *Color imaging array*. 1976.

[54] *Huawei*. URL: https://consumer.huawei.com/cn/ (visited on 01/20/2019).

[55] *Oppo*. URL: https://www.opposhop.cn/ (visited on 01/20/2019).

[56] *Xiaomi*. URL: https://www.mi.com/index.html (visited on 01/20/2019).

[57] *Apple*. URL: https://www.apple.com/ (visited on 01/20/2019).

[58] *APEL Cyclo Olefin Copolymer (COC)*. URL: https://www.mitsuichemicals.com/apel.htm.

[59] *10X DIN Plan Commercial Grade Objective*. URL: https://www.edmundoptics.com/p/10x-din-plan-commercial-grade-objective/5386/.

[60] *Alexa Fluor 488 Technical Information*. 2019. URL: https://www.jacksonimmuno.com/technical/products/conjugate-selection/alexa-fluor/488 (visited on 12/10/2018).

[61] *Optical Filters*. 2019. URL: https://www.chroma.com/products/optical-filters.

[62] *Individual Filters*. 2019.

[63] R H Stover. "Fusarial wilt (panama disease) of bananas and other Musa species". In: *Commonwealth Mycological Institute* (1962), p. 117.

[64] Randy C. Ploetz. "Management of Fusarium wilt of banana: A review with special reference to tropical race 4". In: *Crop Protection* 73 (2015), pp. 7–15. ISSN: 02612194. DOI: 10.1016/j.cropro.2015.01.007. URL: http://dx.doi.org/10.1016/j.cropro.2015.01.007.

[65] Randy C. Ploetz. "Fusarium wilt of banana (Panama disease) in Malawi". In: *Plant Diseases of International Importance* 3 (1992), pp. 270–282.

[66] Buddenhagen L W. "Banana breeding and fusarium wilt". In: *APS Press* (1990), pp. 107–113.

[67] R H Stover. "Disease management strategies and the survival of the banana industry". In: *Annual Review of Phytopathology* 24 (1986), pp. 83–91.

[68] N W Simmonds. *The Evolution of the Bananas*. Longmans, Green, London, 1962, p. 170.

[69] Randy C. Ploetz. "Fusarium Wilt of Banana Is Caused by Several Pathogens Referred to as Fusarium oxysporum f. sp. cubense". In: *Phytopathology* 96.6 (2006), pp. 653–656. ISSN: 0031-949X. DOI: 10.1094/phyto-96-0653.

[70] Randy C. Ploetz. "Panama Disease: An Old Nemesis Rears its Ugly: Head Part 2. The Cavendish Era and Beyond". In: *Plant Health Progress* 7.1 (2006), p. 36. ISSN: 1535-1025. DOI: 10.1094/php-2006-0308-01-rv.

[71] Declan Butler. "Fungus threatens top banana". In: *Nature* 504.7479 (2013), pp. 195–196. ISSN: 0028-0836. DOI: 10.1038/504195a.

[72] F García-Bastidas et al. "First Report of Fusarium oxysporum f. sp. cubense Tropical Race 4 Associated with Panama Disease of Banana outside Southeast Asia". In: *Plant Disease* 98.5 (Oct. 2013), p. 694. ISSN: 0191-2917. DOI: 10.1094/PDIS-09-13-0954-PDN. URL: https://doi.org/10.1094/PDIS-09-13-0954-PDN.

[73] *Colcofluor White Stain*. 2019. URL: https://www.sigmaaldrich.com/catalog/product/sial/18909?lang=en%7B%5C&%7Dregion=US.

[74] Michael V. D'Ambrosio et al. "Point-of-care quantification of blood-borne filarial parasites with a mobile phone microscope". In: *Science Translational Medicine* 7.286 (2015), pp. 1–8. ISSN: 1946-6234. DOI: 10.1126/scitranslmed.aaa3480.

[75] Guoan Zheng, Roarke Horstmeyer, and Changhuei Yang. "Wide-field, high-resolution Fourier ptychographic microscopy". In: *Nature Photonics* 7.9 (2013), pp. 739–745. ISSN: 17494885. DOI: 10.1038/nphoton.2013.187. URL: http://dx.doi.org/10.1038/nphoton.2013.187.

[76] Xiaoze Ou et al. "Quantitative phase imaging via Fourier ptychographic microscopy". In: *Optics Letters* 38.22 (2013), p. 4845. ISSN: 0146-9592. DOI: 10.1364/ol.38.004845.

[77] Zachary F. Phillips et al. "Multi-contrast imaging and digital refocusing on a mobile microscope with a domed LED array". In: *PLoS ONE* 10.5 (2015), pp. 1–13. ISSN: 19326203. DOI: 10.1371/journal.pone.0124938.

[78] Lei Tian and Laura Waller. "Quantitative differential phase contrast imaging in an LED array microscope". In: *Optics Express* 23.9 (2015), p. 11394. ISSN: 1094-4087. DOI: 10.1364/OE.23.011394. URL: https://www.osapublishing.org/abstract.cfm?URI=oe-23-9-11394.

[79] Jeannette Chang et al. "Automated Tuberculosis Diagnosis Using Fluorescence Images from a Mobile Microscope". In: 15.3 (2012), pp. 345–352.

[80] Jerome Mertz. *Introduction to Optical Microscopy*. 2009. ISBN: 0981519482.

[81] Joseph W. Goodman. *Introduction to Fourier Optics*. 3rd ed. 2004. ISBN: 0974707724.

[82] Warren J Smith. *Modern Optical Engineering*. 4th ed. 2007. ISBN: 0071476873.

[83] C. J.R. Sheppard and A. Choudhury. "Image formation in the scanning microscope". In: *Optica Acta* 24.10 (1977), pp. 1051–1073. ISSN: 00303909. DOI: 10.1080/713819421.

[84] D. K. Hamilton, C. J.R. Sheppard, and T. Wilson. "Improved imaging of phase gradients in scanning optical microscopy". In: *Journal of Microscopy* 135.3 (1984), pp. 275–286. ISSN: 13652818. DOI: 10.1111/j.1365-2818.1984.tb02533.x.

[85] Ran Yi, Kengyeh K. Chu, and Jerome Mertz. "Graded-field microscopy with white light". In: *Optics Express* 14.12 (2006), p. 5191. DOI: 10.1364/oe.14.005191.

[86] *Galaxy S9 Specifications*. 2018. URL: https://www.samsung.com/us/smartphones/galaxy-s9/specs/.

[87] Author A S Fruchter and R N Hook. "Drizzle : A Method for the Linear Reconstruction of Undersampled Images". In: *The Astronomical Society of the Pacific* 114.792 (2002), pp. 144–152.

[88] Yih-Chyun Jenq. "Digital spectra of nonuniformly sampled signals. II. Digital look-up tunable sinusoidal oscillators". In: *IEEE Transactions on Instrumentation and Measurement* 37.3 (1988), pp. 358–362.

[89] Shay Maymon and Alan V Oppenheim. "Sinc interpolation of nonuniform samples". In: *IEEE Transactions on Signal Processing* 59.10 (2011), pp. 4745–4758.

[90] Jesus Selva. "Functionally weighted Lagrange interpolation of band-limited signals from nonuniform samples". In: *IEEE Transactions on Signal Processing* 57.1 (2009), pp. 168–181.

[91] Stephen K Park, Robert Schowengerdt, and Mary-Anne Kaczynski. "Modulation-transfer-function analysis for sampled image systems". In: *Applied Optics* 23.15 (1984), pp. 2572–2582.

[92] O Hadar, A Dogariu, and GD Boreman. "Angular dependence of sampling modulation transfer function". In: *Applied Optics* 36.28 (1997), pp. 7210–7216.

[93] Manuel Guizar-Sicairos, Samuel T. Thurman, and James R. Fienup. "Efficient subpixel image registration algorithms". In: *Optics Letters* 33 (2008), pp. 156–158.

[94] *Sony Releases Stacked CMOS Image Sensor for Smartphones with Industry's Highest 48 Effective Megapixels*. 2018. URL: `https://www.sony.net/SonyInfo/News/Press/201807/18-060E/index.html`.

[95] Samsung. *Samsung Introduces Two New 0.8um ISOCELL Image Sensors to the Smartphone Market*. 2018.